



Review

The Recent Advances in the Mechanical Properties of Self-Standing Two-Dimensional MXene-Based Nanostructures: Deep Insights into the Supercapacitor

Yassmin Ibrahim ^{1,†}, Ahmed Mohamed ^{2,†} , Ahmed M. Abdelgawad ³, Kamel Eid ^{3,*} ,
Aboubakr M. Abdullah ^{1,*} and Ahmed Elzatahry ^{4,*}

¹ Center for Advanced Materials, Qatar University, Doha 2713, Qatar; yi1511403@student.qu.edu.qa

² Department of Mechanical and Industrial Engineering, College of Engineering, Qatar University, Doha 2713, Qatar; a.mohamed@qu.edu.qa

³ Gas Processing Center, College of Engineering, Qatar University, Doha 2713, Qatar; aabdelga14@gmail.com

⁴ Materials Science and Technology Program, College of Arts and Sciences, Qatar University, Doha 2713, Qatar

* Correspondence: kamel.eid@qu.edu.qa (K.E.); bakr@qu.edu.qa (A.M.A.); aelzatahry@qu.edu.qa (A.E.)

† These authors contributed equally to this work.

Received: 11 August 2020; Accepted: 2 September 2020; Published: 25 September 2020



Abstract: MXenes have emerged as promising materials for various mechanical applications due to their outstanding physicochemical merits, multilayered structures, excellent strength, flexibility, and electrical conductivity. Despite the substantial progress achieved in the rational design of MXenes nanostructures, the tutorial reviews on the mechanical properties of self-standing MXenes were not yet reported to our knowledge. Thus, it is essential to provide timely updates of the mechanical properties of MXenes, due to the explosion of publications in this field. In pursuit of this aim, this review is dedicated to highlighting the recent advances in the rational design of self-standing MXene with unique mechanical properties for various applications. This includes elastic properties, ideal strengths, bending rigidity, adhesion, and sliding resistance theoretically as well as experimentally supported with various representative paradigms. Meanwhile, the mechanical properties of self-standing MXenes were compared with hybrid MXenes and various 2D materials. Then, the utilization of MXenes as supercapacitors for energy storage is also discussed. This review can provide a roadmap for the scientists to tailor the mechanical properties of MXene-based materials for the new generations of energy and sensor devices.

Keywords: MXene; mechanical properties; 2D materials; metal carbide; young modules; supercapacitors

1. Introduction

Carbon-based nanostructures (C-Ns) such as graphene, carbon nanotubes, and carbon nitride are of great interest due to their unique physicochemical merits such as high surface area, thermal stability, and outstanding mechanical properties [1–4]. These properties promoted the utilization of C-Ns in structural composites, protective coatings, fibers, energy storage, catalysis, and durable wearable sensors; however, their complicated fabrication process remains a major challenge [5–7]. Y. Gogotsi and M.W. Barsoum groups discovered a novel family of 2D transition metal carbides or nitrides called MXene (pronounced “maxenes”) [8]. The general formula of MXene is $M_{n+1}X_nT_x$ ($n = 1–4$), where M represents transition metals, A is an A-group element of group 13 to 15 in the periodic table, X is carbon or nitrogen, and T_x is surface functional groups (OH, O, Cl, F) (Scheme 1) [8]. There are around three main structures of MXenes, including M_2XT_x , $M_3X_2T_x$, and $M_4X_3T_x$, derived from the selective etching

of MAX phases (M, A, and X elements are in Scheme 1) including M_2AX , M_3AX_2 , and M_4AX_3 . To this end, more than 30 MXenes compositions have prepared, such as Ti_2CT_x , Nb_2CT_x , V_2CT_x , $Ti_3C_2T_x$, $Mo_2TiC_2T_x$, $Mo_2Ti_2C_3$, $Ti_yNb_{2-y}CT_x$, and $Nb_yV_{2-y}CT_x$, along with additional dozens were explored by computational methods [9–11].

MXenes possess unique physical and chemical merits such as great miscibility, high surface area to volume ratio, accessible active sites, surface charge state, electron-rich density, and absorption of electromagnetic waves [12]. This is besides the impressive properties of 2D carbide transition metal carbides/nitrides, such as multilayered structures with excellent mechanical properties, strength, flexibility, and high electrical conductivity [12]. Additionally, the fabrication process of MXene is scalable, productive, controllable, facile, and feasible for large-scale applications [12]. MXenes with high negative zeta potential are miscible in various solvents, polymeric materials, and other C-Ns materials resulting in the formation of unlimited composites with various properties [13]. The impressive mechanical properties of MXenes are one of the unique features for MXene [2,14–16]. Despite the significant progress in the synthesis of MXene nanostructures, $Ti_3C_2T_x$ compound is the most widely studied material, for various applications, due to its impressive electrical conductivity, mechanical properties, and electrochemical properties electromagnetic shielding [2,14–16].

There are numerous published reviews in the fields of MXenes for energy, catalysis, and environmental remediation [12,17–23]. However, the reviews on the mechanical properties of self-standing MXenes are not yet reported [24]. Many studies have shown that MXenes exhibits excellent mechanical ion adsorption properties, which in turn will set the stage for exploring the possibility of their use in sensors and flexible devices [6,24–26]. For instance, the strain-tunable electrochemical properties of MXenes enable them to be a propitious solution for flexible and stretchable devices [6,24–26]. Regarding the electrochemical properties of MXenes, their large specific surface area makes them a promising candidate for various applications such as supercapacitor, Li-ion and Sodium-ion batteries, hydrogen storage, adsorption, and catalysts [6,24–26]. Due to the abundant research and ceaseless publications on the mechanical properties of MXene (more than 146 articles, according to SciFinder), it is crucial to provide a timely update of research efforts in this area.

Inspired by this, the presented review summarizes the recent progress of research work on the mechanical properties of self-standing MXenes, from both theoretical and experimental views. This includes: (1) elastic properties and superior strengths, (2) bending rigidity, (3) adhesion, and sliding resistance with their fundamental mechanism supported with numerous representative paradigms. Also, there are deep insights into the utilization of MXenes as supercapacitors. The future perspective of the mechanical applications of MXene is also discussed.

1 H Hydrogen 1.008																	2 He Helium 4.003
3 Li Lithium 6.941	4 Be Beryllium 9.012											5 B Boron 10.811	6 C Carbon 12.011	7 N Nitrogen 14.007	8 O Oxygen 15.999	9 F Fluorine 18.998	10 Ne Neon 20.180
11 Na Sodium 22.990	12 Mg Magnesium 24.305											13 Al Aluminum 26.982	14 Si Silicon 28.086	15 P Phosphorus 30.974	16 S Sulfur 32.066	17 Cl Chlorine 35.453	18 Ar Argon 39.948
19 K Potassium 39.098	20 Ca Calcium 40.078	21 Sc Scandium 44.956	22 Ti Titanium 47.867	23 V Vanadium 50.942	24 Cr Chromium 51.996	25 Mn Manganese 54.938	26 Fe Iron 55.845	27 Co Cobalt 58.933	28 Ni Nickel 58.693	29 Cu Copper 63.546	30 Zn Zinc 65.38	31 Ga Gallium 69.723	32 Ge Germanium 72.64	33 As Arsenic 74.922	34 Se Selenium 78.971	35 Br Bromine 79.904	36 Kr Krypton 84.798
37 Rb Rubidium 84.468	38 Sr Strontium 87.62	39 Y Yttrium 88.906	40 Zr Zirconium 91.224	41 Nb Niobium 92.906	42 Mo Molybdenum 95.95	43 Tc Technetium 98.907	44 Ru Ruthenium 101.07	45 Rh Rhodium 102.906	46 Pd Palladium 106.42	47 Ag Silver 107.868	48 Cd Cadmium 112.414	49 In Indium 114.818	50 Sn Tin 118.710	51 Sb Antimony 121.760	52 Te Tellurium 127.6	53 I Iodine 126.905	54 Xe Xenon 131.294
55 Cs Cesium 132.905	56 Ba Barium 137.328	57-71	72 Hf Hafnium 178.49	73 Ta Tantalum 180.948	74 W Tungsten 183.84	75 Re Rhenium 186.207	76 Os Osmium 190.23	77 Ir Iridium 192.227	78 Pt Platinum 195.085	79 Au Gold 196.967	80 Hg Mercury 200.592	81 Tl Thallium 204.383	82 Pb Lead 207.2	83 Bi Bismuth 208.980	84 Po Polonium (209)	85 At Astatine (210)	86 Rn Radon (222)
87 Fr Francium 223.020	88 Ra Radium 226.025	89-103	104 Rf Rutherfordium (261)	105 Db Dubnium (262)	106 Sg Seaborgium (266)	107 Bh Bohrium (264)	108 Hs Hassium (265)	109 Mt Meitnerium (268)	110 Ds Darmstadtium (269)	111 Rg Roentgenium (272)	112 Cn Copernicium (277)	113 Nh Nihonium unknown	114 Fl Flerovium (289)	115 Mc Moscovium unknown	116 Lv Livermorium (293)	117 Ts Tennessine unknown	118 Og Oganesson unknown

Scheme 1. The composition of MXenes and MAX phases from the periodic table.

2. Mechanical Properties of Self-Standing MXenes

In this section, the elastic properties and superior strengths of self-standing MXenes are briefly summarized, and we discuss the effect of other parameters such as layer thickness, functional groups, and presence of point defects, different transition metals, and substitutional doping. The mechanical properties of MXenes with different compositions are summarized in Table 1.

Table 1. The mechanical properties of MXenes with different compositions.

Materials	Morphology	Preparation Method (Experimentally/Theoretically)	Measurements	Elastic Constants c_{11} [GPa]	Young's Modulus E [GPa]	Strains along Uniaxial x (ϵ_x)	Strengths along Uniaxial x (σ_x) [GPa]	Ref.
Ti ₃ C ₂ H ₂	2D unit cell	Theoretical calculations	VASP/PBE	419	392	-	-	[27]
Zr ₃ C ₂ O ₂	2D hexagonal lattice	Etching Al layers in Zr ₃ AlC ₅	DFT	392.9	-	-	-	[28]
Ti ₂ C	2D sheets	Theoretical calculations	VASP	609	-	-	-	[29]
Ti ₂ CO ₂	2D sheets	Theoretical calculations	Nanoindentation process	-	983	-	-	[30]
Ta ₂ C	2D sheets	Theoretical calculations	CASTEP/Wu-Cohen	788	-	-	-	[31]
Ti ₂ C	2D sheets	Theoretical calculations	MD	-	597	-	-	[32]
Mo ₂ C	2D sheets	Chemical vapor deposition	VASP	-	312	-	-	[33]
Ti ₂ CO ₂	2D sheets	Etching Al layers in Ti ₂ AlC ₂	VASP/PBE	745	570	0.28	56	[34]
W ₂ C	2D sheets	Theoretical calculations	VASP/PBE	781.9	-	0.16	65.6	[35]
Materials	Morphology	Preparation method	Measurements	c_{11} (N/m)	E (N/m)	ϵ_x	σ_x (N/m)	Ref.
Ti ₃ C ₂ O ₂	2D unit cell	Theoretical calculations	VASP/PBE	379	347	-	-	[27]
W ₂ HfC ₂ O ₂	2D unit cell	Theoretical Calculations	VASP/PBE	-	-	-	47.3	[34]
Mo ₂ CO ₂	hexagonal unit cell	Theoretical calculations	VASP/PBE	361	302	-	-	[35]
Ti ₂ CO ₂	2D sheets	Theoretical Calculations	DFT	-	241	0.24	30.7	[36]

2.1. Elastic Properties and Ideal Strengths

2.1.1. Effect of Functional Terminations

Functional terminations ($-O$, $-F$, $-OH$) of carbides have a significant effect on the structural and mechanical properties of MXenes, as demonstrated extensively by DFT calculation. Figure 1a shows the variation of the calculated elastic constants c_{11} of M_2CT_2 MXenes as a function of the layer thickness and different functional terminations [27]. It can be seen that, except for Cr_2CO_2 , the elastic constant for MXenes with oxygen functionalization showed higher elastic constants compared to those with hydroxyl and fluorine functional groups [27]. This is due to the stronger interaction between the oxygen and surface M atoms [27].

The stress-strain curves, as well as the deformation mechanisms, were investigated in response to tensile stress by DFT calculation for 2D $Ti_{n+1}C_n$ ($n = 1-3$) (Figure 1b) [37]. Three loading conditions were considered to measure the intrinsic mechanical responses to tensile strain in 2D Ti_2C , which are biaxial tension, uniaxial tension along the x -direction, and the y -direction [37]. The stress-strain relations for 2D Ti_2C under different loading conditions are shown in (Figure 1b) [37]. It was found that 2D Ti_2C is an elastically isotropic material, since the corresponding Young's modulus E_x and E_y were estimated to be 620 GPa and 600 GPa, respectively [37]. Moreover, 2D Ti_2CO_2 can sustain higher strains for the three loading conditions than 2D Ti_2C , which is even higher than that of graphene due to surface functionalizing oxygen [37]. Another large variation in mechanical properties was detected when different transition metal, along with surface functional groups, are used [28,38]. Furthermore, in comparison to other functional groups in Ti_3C_2 , the oxygen group possesses the highest in-plane planar elastic modulus, as shown in (Figure 1c–e), leading to enhancement of strength, and adsorption energy, which indicates its good thermodynamic stabilization [39]. This can be attributed to the significant charge transfer from inner to outer surface bonds [39].

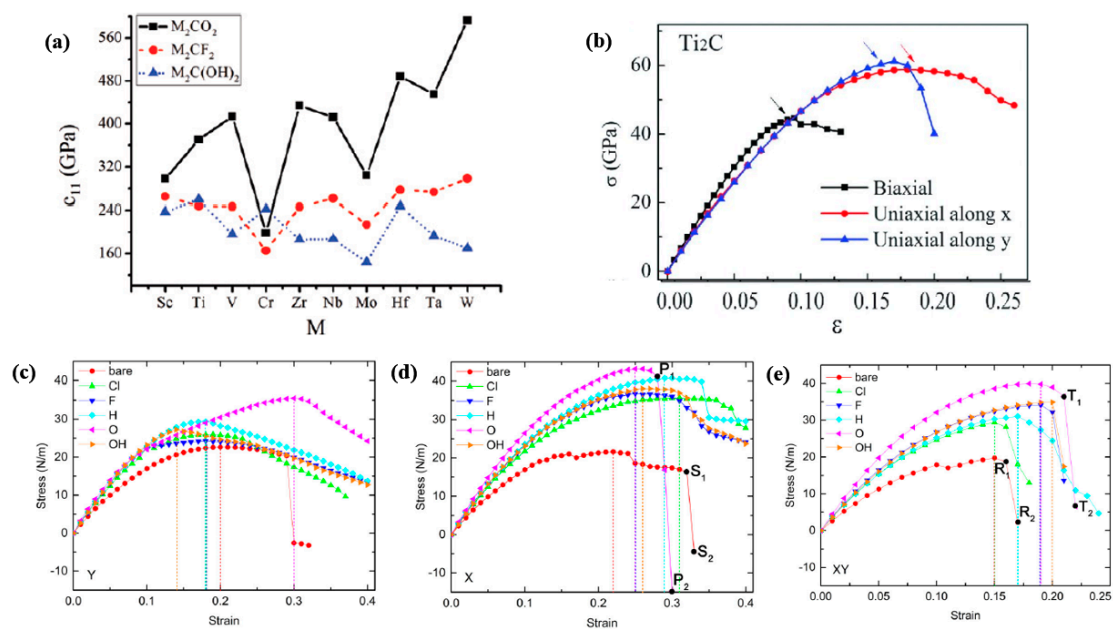


Figure 1. (a) The elastic constants of c_{11} for M_2CT_2 MXenes. Reproduced with permission from [27]. Copyright IOP Publishing, 2015. (b) Calculated stress-strain curves of 2D Ti_2C . Reproduced with permission from [37]. Copyright RSC, 2015 (c) The stress-strain curves in the uniaxial tension Y direction, (d) The stress-strain curves in the uniaxial tension X direction for Ti_3C_2 and P_1 and P_2 for $Ti_3C_2O_2$, (e) The stress-strain curves in biaxial tension for Ti_3C_2 and T_1 and T_2 for $Ti_3C_2O_2$. All the vertical lines mention the maximum stress values. Reproduced with permission from [39]. Copyright APS, 2016.

The effect of surface termination groups on the elastic constants of 2D Ti_2CT_2 and $Ti_3C_2T_2$ was investigated using first-principles calculation by Density-functional theory (DFT) simulation [40]. It was found that the stiffness is highly dependent on the termination group. The elastic stiffness of the MXenes is only maintained in the case of MXenes with O terminations while deteriorates in the case of F and OH terminations [40]. This can be explained by the in-plane lattice constant in the 2D MXenes with different termination groups. The in-plane lattice constant for both 2D Ti_2CT_2 and $Ti_3C_2T_2$ MXenes was shortest in the case of O termination. In contrast, F and OH termination had larger in-plane lattice constants indicating a strong interaction between Ti and terminating O atoms.

Another work in the literature [30] studied the effect of surface groups on the elastic properties of MXenes. The ionic mobility for MXenes with different termination groups was investigated under different strain conditions, using multiaxial loading schemes, biaxial and uniaxial tension along x-direction and y-direction. It was observed that Ti_2C (Ti_2CF_2) (Ti_2CO_2) can tolerate percentage of strains of 8 (20) {19}, 16 (29) {24}, and 18 (10) {29} under biaxial and uniaxial tensions along the x and y directions, respectively. Whereas Zr_2C (Zr_2CF_2) (Zr_2CO_2) can withstand strains of 12 (21) {21}%, 16 (29) {27}% and 17 (16) {28}%, respectively as shown in Figure 2 [30]. It can be seen that Ti_2CO_2 has higher critical strains than both Ti_2C and graphene [30]. Additionally, overall, the surface groups (O and F) increase the critical strain and provide more mechanical flexibility to the 2D MXenes by considerably slowing down the collapse of the transition metal layers. This makes MXenes with O and F termination groups potential candidates for high-performance lithium-ion batteries [30]. A recent study [32] investigated the effect of point defects on the elastic properties of MXenes using the atomistic simulation of nanoindentation of $Ti_{n+1}C_nO_2$ monolayer. The Young's modulus of $Ti_3C_2O_2$ was found to be 466 GPa, which is slightly lower than the obtained values by DFT and hybridized computational molecular dynamics (MD) simulations of 523 [41] and 502 [42] GPa, respectively. This can be attributed to the presence of surface terminations. Moreover, the breaking strength of $Ti_3C_2O_2$ was calculated as 25.2 N/m, lower than that of graphene (42 N/m) [43]. As seen in (Figure 3a,b), Ti_2CO_2 exhibited a more sudden fracture compared to $Ti_3C_2O_2$, at higher force and lower displacement [32]. This can be explained by the presence of two fewer atomic layers in Ti_2CO_2 , resulting in a decreased resistance and more abrupt failure. The calculated elastic modulus of Ti_2CO_2 (983 GPa) is higher than that of $Ti_3C_2O_2$ and almost approaching the value of graphene [32]. However, this value is inconsistent with the previously reported values by DFT (636 GPa) [41] and hybridized MD (597 GPa) [42]. The calculated breaking force for Ti_2CO_2 of 33.6 N/m is approaching the levels of graphene [32].

Figure 3c–f shows simulation results of the nanoindentation of $Ti_3C_2O_2$ with titanium and carbon vacancies (V_{Ti} and V_C , respectively) [32]. It can be seen that the cracks failed to propagate to the edges of the samples contained 1% V_{Ti} and 10% V_C with the same extent of the pristine $Ti_3C_2O_2$, which explains the effect of defects on the fracture mechanism of the sheets [32]. Furthermore, the presence of defects results in a 17% reduction in elastic modulus (386 GPa), which is still higher than graphene oxide and in good agreement with the recent experimental studies [2].

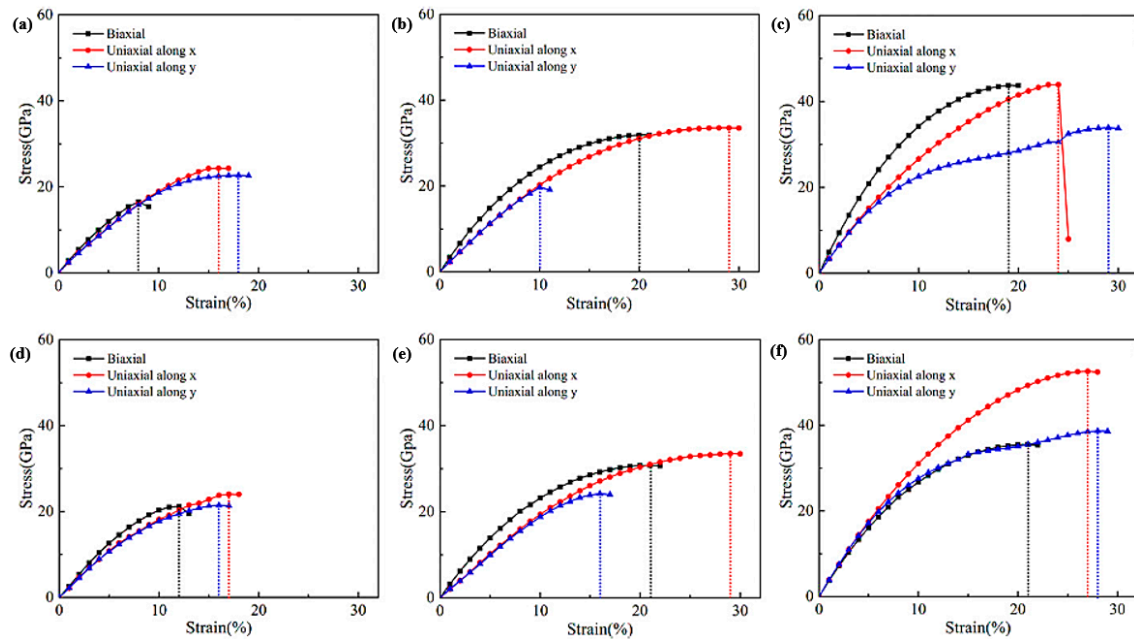


Figure 2. Strain-stress relationships for (a) Ti_2C , (b) Ti_2CF_2 , (c) Ti_2CO_2 , (d) Zr_2C , (e) Zr_2CF_2 , and (f) Zr_2CO_2 under both biaxial and uniaxial load conditions. Reproduced with permission from [30]. Copyright PNAS, 2017.

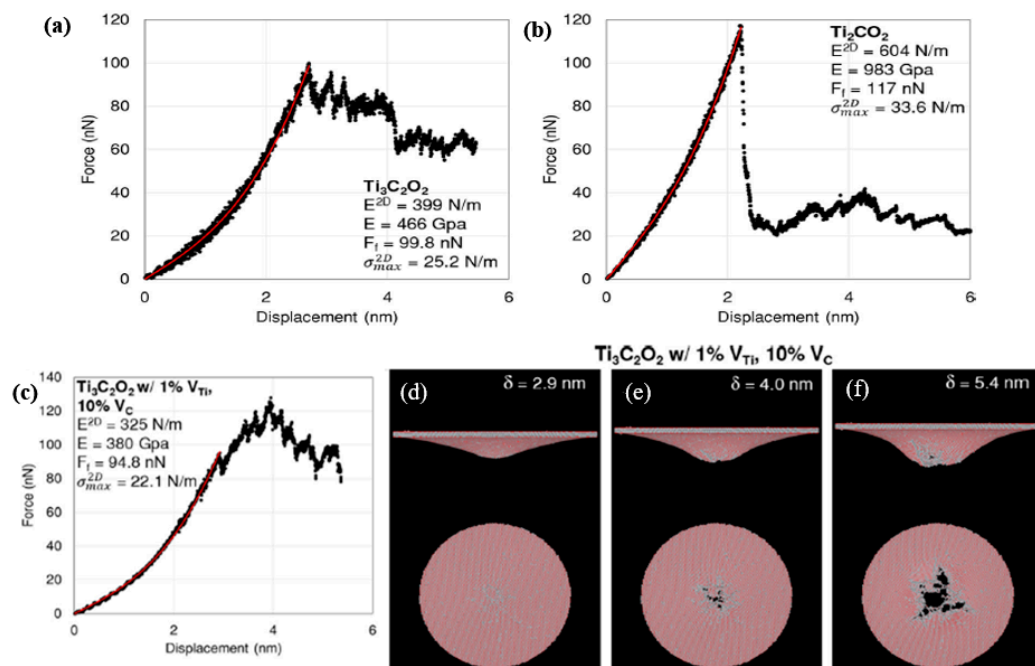


Figure 3. Force-Displacement curves for pristine monolayers of $\text{Ti}_3\text{C}_2\text{O}_2$ (a) and Ti_2CO_2 (b). (c) A representative force-displacement curve. (d-f) photographs are showing the progressive indentation and fracture of the same representative $\text{Ti}_3\text{C}_2\text{O}_2$ monolayer with 1% V_{Ti} and 10% V_{C} . Reproduced with permission from [32] Copyright Elsevier, 2019.

2.1.2. Effect of the Mass of the Transition Metal

DFT calculation using the Vienna ab initio simulation package (VASP) code, the mechanical and dynamical properties were obtained for both pristine and terminated MXene (M_2XT_2) structures with $\text{M} = \text{Sc}, \text{Mo}, \text{Ti}, \text{Zr}, \text{Hf}$, $\text{X} = \text{C}, \text{N}$, and $\text{T} = \text{O}, \text{F}$ [29]. It was found that for the pristine carbides, unlike nitride-based pristine, there is a positive correlation between the stiffness and the mass of the

transition metal, as indicated by elastic constants [29]. Moreover, the Young Modulus for the nitrides was slightly higher than that of the carbides [29].

In a recent study [44], the effect of asymmetrical functionalization of F and OH groups on the mechanical properties of monolayer Janus MXenes M_2X ($M = \text{Sc, Ti, V, Mn, Nb, Mo, Hf}$; $X = \text{C, N}$) where the X atomic layer is sandwiched between 2 M layers was studied via DFT. It was found that mechanical properties depend on the mass of the transition metal and the surface functionalization. Results show that asymmetric functionalization has a consequential effect on the elastic properties of the MXenes. For all the pristine M_2X , the in-plane stiffness C of M_2C is slightly lower than that of M_2N due to the additional valence electron that the N atom provides than C atoms than in turn generate stiffer M-X bonds. However, due to the H structure of Mo_2X , the in-plane stiffness of Mo_2N is slightly lower than that of Mo_2C . Another finding was that by asymmetrical F/OH surface functionalization, the in-plane stiffness C of Sc_2C was increased from 92 Nm^{-1} to 192 Nm^{-1} , which agrees with what was found by [45]. Moreover, the in-plane stiffness C of monolayer M_2X is lower than that of both graphene [46] and single layer h-BN [47]. Upon asymmetrical surface functionalization, the mechanical stability and the in-plane stiffness C of monolayer M_2X can be enhanced [44]. Despite the fact that it is experimentally challenging to synthesize MXenes accompanied with mixed functional groups [48], eventually, the Janus MXenes could be synthesized experimentally, similar to the Janus graphene [33] and Janus graphene oxide [49].

2.1.3. New Types of MXenes

The enhanced mechanical properties of new types of MXenes, such as Mo_2C were predicted by DFT calculations [34]. The Mo_2C was fabricated via the chemical vapor deposition (CVD) method, where the carbon source was methane, and Cu-foil was selected to be the substrate for a molybdenum foil [50]. The lateral size of the fabricated Mo_2C was found to be $>100 \mu\text{m}$ [50]. No significant structural changes were observed after immersing Mo_2C in several solvents such as isopropanol, ethanol, HCl, or after thermal annealing in air at $200 \text{ }^\circ\text{C}$ for 2 h, indicating its thermal and chemical stability [50]. Compared to the MoS_2 , Mo_2C had a slightly higher biaxial elastic modulus of $312 \pm 10 \text{ GPa}$ [34]. The relatively large elastic modulus could be explained by the strong interactions between Mo and C atoms. The calculated stress-strain curve for Mo_2C (Figure 4a) shows mostly an elastic response until a critical strain of 0.086, then the Mo_2C exhibited creep deformation. Although this critical strain is less than that of MoS_2 , the ideal strength of Mo_2C is predicted as 20.8 GPa, approaching the value of a monolayer of MoS_2 (23.8) GPa [34]. The impressive mechanical properties make Mo_2C a potential candidate for mechanical applications.

2.1.4. Effect of Doping

The effect of doping on the elastic properties of MXenes was investigated by DFT calculations [51]. Specifically, B and V atoms were substitutionally doped into Ti and C sites in Ti_2C , respectively, resulting in $Ti_2(C_{0.5}B_{0.5})$ and $(Ti, V)C$. While V-doping results only in marginal enhancement, B-doping yields improved the elastic properties by decreasing the in-plane Young's modulus and the yield strength. The reduction in the stiffness can be attributed to the weak-bond of Ti-B compared to the Ti-C bond (Figure 4b,c) [51]. Figure 5 shows the calculated stress-strain curves using the non-magnetic (NM) and the lowest energy antiferromagnetic (AFM) states [51]. It can be seen that a remarkable decrease of about 25–27% in Young's modulus and in-plane stiffness of $Ti_2(C_{0.5}B_{0.5})$ compared to Ti_2C . However, the doping of V at Ti sites results in the same stiffness of the undoped Ti_2C . Intriguingly, the stiffness of $Ti_2(C_{0.5}B_{0.5})$ was about 4.2, 1.5, 1.86, and 3.1 times higher than that of 2D MoS_2 , graphene, h-BN, and SiC reported elsewhere, respectively, due to the B-doping effect [51,52]. In contrast, $Ti_2(C_{0.5}B_{0.5})$ and $(Ti, V)C$ with O-termination groups exhibited improved elastic properties compared to undoped Ti_2C O-passivated or O-free, owing to the enhancement of the local strain, causing a consequent enlarging of the average thickness of O-passivated MXene by nearly 2% [51].

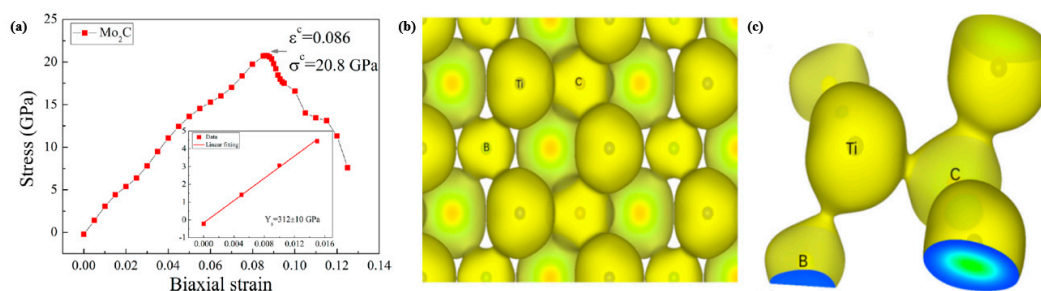


Figure 4. (a) Calculated stress versus biaxial strain for the Mo_2C . Reproduced with permission from [34]. Copyright ACS Publications, 2016. (b) Shows the plot in an extended region, (c) zoomed view focused on central Ti atom bonded with B and C. The stronger covalency of the Ti-C bond compared to the Ti-B bond is visible. Reproduced with permission from [51]. Copyright AIP Publishing, 2017.

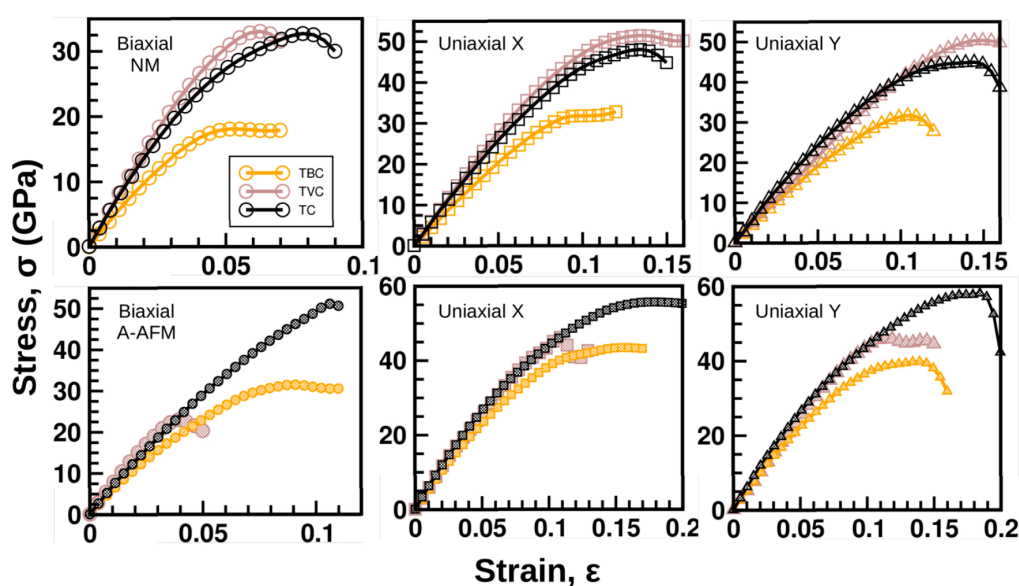


Figure 5. The stress-strain curve of Ti_2C , $\text{Ti}_2(\text{C}_{0.5}\text{B}_{0.5})$ and $(\text{Ti}, \text{V})\text{C}$ under biaxial and uniaxial tensile strains along with the X and Y directions. The top panels show the results for NM states, while the bottom panels show the results for the minimum energy AFM magnetic state. Reproduced with permission from [51]. Copyright AIP Publishing, 2017.

Another study [53] predicted enhanced elastic properties of a 2D Tungsten Carbide (W_2C) monolayer by DFT calculations. The calculated c_{11} of 781.9 GPa indicated that W_2C is mechanically stable as it satisfies the 2D materials criteria for mechanical stability [36]. The uniaxial tensile loading was applied along the armchair direction, where the correlation between the strain and stress was investigated. As the strain increases, the stress increases until approaching the ultimate tensile strength, as shown in (Figure 6a), then it decreases gradually. The same trend goes for the calculations along the zigzag direction. The calculated ultimate strength of W_2C is comparable to Ti_2C [37] but higher than that of MoS_2 [54]. The Young's modulus of W_2C along with the armchair and zigzag directions are 648 and 645 GPa, respectively, compared to graphene (1000 GPa) [43] and Ti_2C (600 GPa) [37]. Furthermore, W_2C was observed to have a high negative Poisson's ratio (NPR) as they exhibited a positive strain along the longitudinal direction while applying stretching force on the transverse direction (Figure 6b) [53]. This intrinsic NPR of W_2C could be explained by the robust coupling between C-p and W-d orbitals in the pyramid structural unit. Additionally, incorporating the surface functional groups to the calculations show that the NPR of W_2C was turned into PPR due to the weakening of M-C interactions [53].

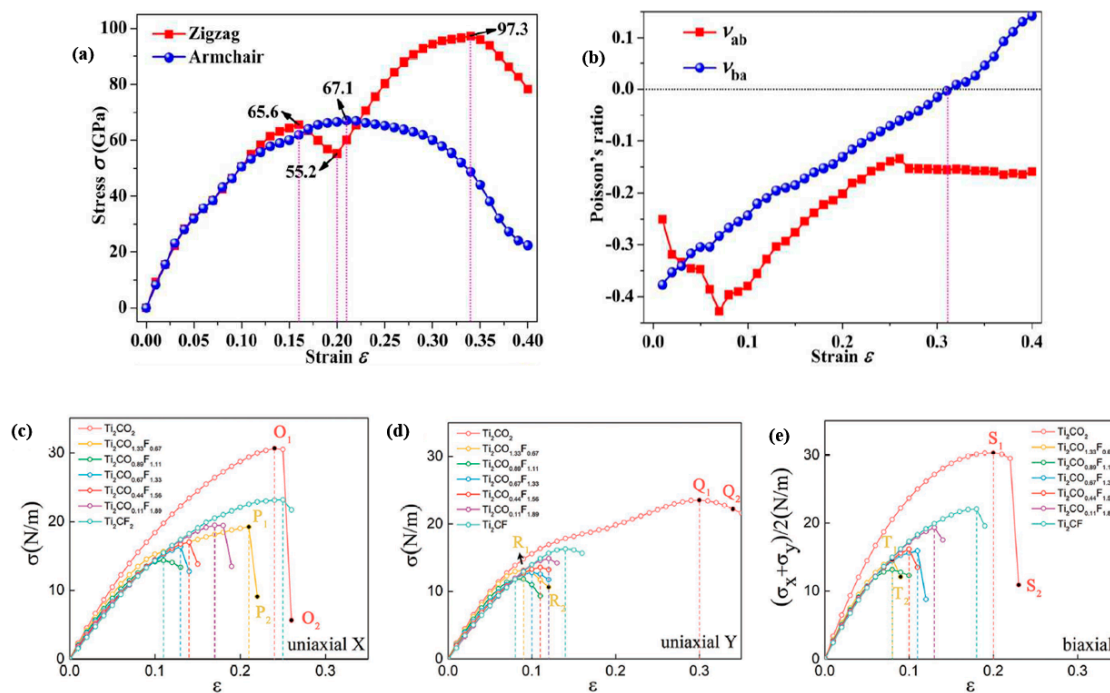


Figure 6. (a) Stress-strain curves of intrinsic W₂C under uniaxial stretching, (b) Poisson's ratios of W₂C stretched along with different directions. Reproduced with permission from [53]. Copyright RSC, 2018. The calculated stress σ versus strain ϵ curves for Ti₂CT₂ with pure and mixed terminations under (c) uniaxial x , (d) uniaxial y , and (e) biaxial loading conditions. Reproduced with permission from [55]. Copyright John Wiley & Sons, 2018.

2.1.5. Effect of Varying F/O Ratio

The mechanical properties of Ti₂CT_n terminated by O- and F- were manipulated by varying F/O ratio from 1:17 to 17:1 [55]. The mechanical properties of the five thermodynamically most stable structures with F/O ratios 1: 2, 5:4, 2:1, 7:2, and 17:1 were investigated. It was noticed that as the F/O ratio increases, the Young's, along the x - and y -directions, and shear moduli of Ti₂CT₂ gradually decrease. For instance, Young's modulus along the x -direction decreased from 222 to 159 (N m⁻¹), while the shear modulus decreased from 88 to 58 (N m⁻¹). Additionally, all the Ti₂CT₂, with pure and a mixture of surface terminations, exhibited Poisson ratios greater than that of graphene (0.224), ranging from 0.24 to 0.37. Ti₂CO_{1.33}F_{0.67} exhibits the highest Young's modulus along the x -direction (222 N m⁻¹), among other Ti₂CT₂, which is comparable to Ti₂CO₂ (241 N m⁻¹). The calculated stress-strain curves shown in (Figure 6c–e) indicated that Ti₂CO₂ (24%, 30%, and 20% under uniaxial tensions along the x - and y -directions and under biaxial tensions) and Ti₂CF₂ (25%, 14%, and 18%) have higher critical strains than that of Ti₂CT₂ with mixed terminations. Thus, the mechanical flexibility could be decreased with mixed functional groups. Moreover, a lower critical strain of Ti₂CT₂ is observed with a higher degree of the mixture (Figure 6c–e), such as in Ti₂CO_{0.11}F_{1.89}, which could sustain only the lowest critical strains. A similar trend is seen for the ideal strength with the variation of the degree of mixture, indicating that the best mechanical strengths are assigned to Ti₂CO_{1.33}F_{0.67} and Ti₂CO_{0.11}F_{1.89}. These findings pave the way to demonstrate more effective methods in tuning the electrochemical properties of MXenes by strains.

2.1.6. Effect of Number of Layers and Layer Thickness

The elastic modulus and breaking strength of monolayer and bilayer Ti₃C₂T_x flakes were experimentally determined by AFM indentation [2]. It was shown that E^{2D} values determined for bilayer Ti₃C₂T_x flakes are exactly twice that determined for monolayer MXene membranes, suggesting strong interaction between the layers due to hydrogen bonding. A single layer of Ti₃C₂T_x has an

effective Young's modulus of approximately 333 GPa, which is higher than that of graphene oxide (210 GPa) and some other MXenes. Meanwhile, the breaking strength of a single layer of $\text{Ti}_3\text{C}_2\text{T}_x$ was 17.3 ± 1.6 GPa. It was noted that Young's modulus obtained experimentally is lower than that from the MD simulation due to the presence of defects and surface functionalization.

The effect of layer thickness on the structural and elastic properties of 2D $\text{Ti}_{n+1}\text{C}_n$ was studied using MD calculations [42]. It was demonstrated that the Young's modulus of MXenes could be significantly increased by decreasing the layer thickness. The Young's modulus of Ti_2C , Ti_3C_2 , and Ti_4C_3 was found to be 597, 502, and 534 GPa, respectively, with a strain ε less than 0.01 and within 10% interpolation error. As observed, the highest Young's modulus was reported to the thinnest Ti_2C carbide (3 atomic layers). These results are in agreement with other theoretical predictions from DFT [41].

Similar findings on the effect of monolayer thickness on the elastic properties of the carbide ($\text{Ti}_{n+1}\text{C}_n$) and nitride-based ($\text{Ti}_{n+1}\text{N}_n$) MXenes, by DFT calculations, were reported in another study [53]. It was shown that increasing the monolayer thickness decreases Young's moduli of MXenes. The Young's moduli of the $\text{Ti}_{n+1}\text{C}_n$ were found to be 601, 473, and 459 GPa for Ti_2C , Ti_3C_2 , and Ti_4C_3 , respectively, which is in good agreement with the values obtained previously by DFT calculations [37]. The bulk model was generated by increasing the layer of atoms to infinity, thus showing that bulk $\text{Ti}_{n+1}\text{C}_n$ has Young's modulus of 433 GPa, lower than that of rest of $\text{Ti}_{n+1}\text{C}_n$ MXenes. Although a similar trend was observed for the $\text{Ti}_{n+1}\text{N}_n$, higher Young's moduli of $\text{Ti}_{n+1}\text{N}_n$ over $\text{Ti}_{n+1}\text{C}_n$ was observed, which is consistent with previously reported experimental measurements for bulk TiN [56] and bulk TiC [57,58]. Furthermore, due to the 2D morphology of $\text{Ti}_{n+1}\text{C}_n$ and $\text{Ti}_{n+1}\text{N}_n$ with lower thickness, their calculated in-plane Poisson's ratios (ν) are 0.25 and 0.26, higher than that of the bulk TiC and TiN (~ 0.23) [56–58], which is indicative of increased elasticity.

2.1.7. Effect of Intercalated Ions and Electrolytes

In order to study the effect of the intercalated ions on the mechanical properties of MXenes, the mechanical properties were characterized at the nanoscale instead of at the macroscopic scale [59]. The elastic changes of a 2D $\text{Ti}_3\text{C}_2\text{T}_x$ based electrode in a direction normal to the basal plane were studied via in-situ contact resonance force microscopy (CRFM) imaging, combined with DFT during alkaline cation intercalation/extraction [59]. The DFT calculations agreed well with experiments since the presence of only 12.5% H_2O resulted in a drastic decrease of E from 126 GPa of the dry sample to 29 GPa. The out-of-plane elastic modulus significantly correlated with the cations content. The MXene electrode exhibited shrinkage of almost 10% (Figure 7a) in its lattice structure associated with a decrease in the interlayer distance after Li^+ intercalation [59].

The $\text{Ti}_3\text{C}_2\text{T}_x$ exhibited smaller volume changes when K^+ ions were intercalated, resulting in lower stiffness than in the case of Li^+ ions [59]. This is possible because the stiffness of the cation/water/MXene system is enhanced by the strong oxygen atoms bonds resulted from one hydrogen atom, from the surface hydroxyl group, being pushed out by the cations. Higher CR frequency values after Li^+ intercalation indicates a stiffer 2D structure, in the direction normal to the electrode surface, with elastic moduli ranging between 5 and 18 GPa (Figure 7b,c), twice that of water [59]. Additionally, it was found that the elastic modulus can be tuned using the right combination of the electrolyte and the electrode. The use of both the CRFM technique and DFT calculations revealed that the interface between the electrode/electrolyte could be controlled by probing the mechanical properties associated with the cation storage for applications such as supercapacitors and various types of batteries [59].

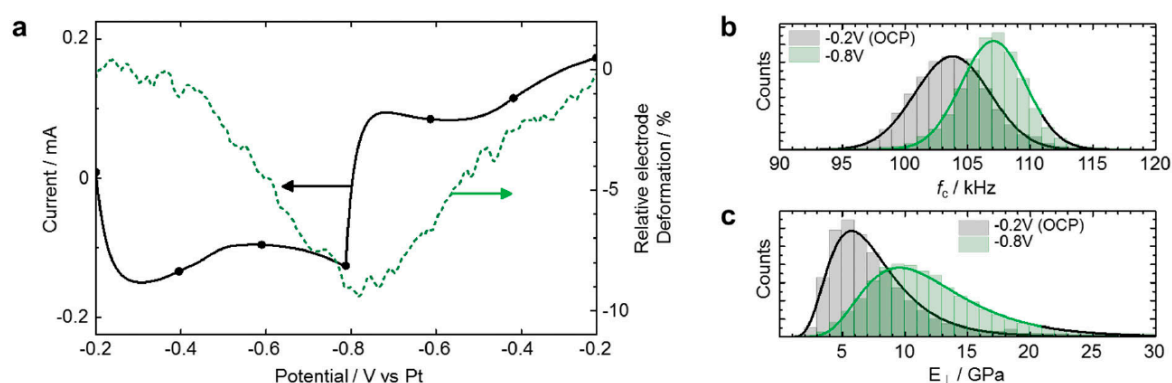


Figure 7. Elastic changes of $\text{Ti}_3\text{C}_2\text{T}_x$ in Li_2SO_4 electrolyte. (a) Electrochemical profile of Li^+ intercalation/extraction showing the current and single point relative electrode deformation profiles as a function of potential. (b) Frequency distribution histograms at charged and discharged states. (c) Corresponding elastic modulus distribution histograms. Reproduced with permission from [59]. Copyright John Wiley & Sons, 2016.

2.2. Bending Rigidity

The mechanical response of 2D materials obtained under bending deformations is a critical quantity called the bending rigidity [24]. The bending rigidity of MXenes is poorly investigated. To the best of our knowledge, only two papers discussing this quantity have been published so far. The bending rigidity is also affected by some parameters, such as the layer thickness and the functionalization group. The bending rigidity of MXenes was first quantified in 2018 using classical MD simulation for three different 2D titanium carbides (Ti_2C , Ti_3C_2 , and Ti_4C_3) to demonstrate their bending resistance under applied bending load [60]. Ti_2C was found to possess higher resistance for bending than atomically thin graphene due to its larger thickness. In contrast, the bending strength of Ti_2C is lower than that of MoS_2 due to different atomic arrangements and larger thickness in MoS_2 compared to Ti_2C [60].

DFT calculations have shown that the in-plane stiffness (C) and out-of-plane bending rigidity (D) of Ti_2CT_x , $\text{Ti}_3\text{C}_2\text{T}_x$, Nb_2CT_x , and $\text{Nb}_4\text{C}_3\text{T}_x$ ($T = \text{O}, \text{OH}, \text{and F}$) are highly dependent on the layer thickness of $[\text{M}_{n+1}\text{X}_n]$ and functionalization groups [61]. As the $[\text{M}_{n+1}\text{X}_n]$ layer thickness increases, the in-plane stiffness increases (Figure 8a) due to the increase in the number of M-C bonds [61]. Nb_2CT_2 and Ti_2CT_2 have relatively low in-plane stiffness due to having only a three-atomic layer in $[\text{M}_2\text{X}]$, compared to seven-atomic-thick $[\text{Nb}_4\text{C}_3]$ layer in $\text{Nb}_4\text{C}_3\text{T}_2$ with the largest in-plane stiffness. Moreover, the surface terminations in MXenes significantly increased the stiffness (Figure 8a) [61]. The O-functionalized MXenes were found to have higher in-plane stiffness than that of bare MXenes due to the strong O–M bonding. However, similar in-plane stiffness was noticed for OH, and F terminated MXenes [61]. Figure 8b depicts the bending rigidities of the four MXenes and their functional groups, showing that Ti_2C has a D value of 4.47 eV [61]. Compared to MXenes, the surface terminations groups decreased their stiffness of graphene and graphene oxides [62,63]. Additionally, the measured bending rigidities of Ti_2C with surface functionalities (4.47 eV) were relatively lower than the previously reported value by MD calculations (5.21 eV) [61], but was higher than that of a graphene monolayer (1.2 eV) [64]. Meanwhile, three-atom-thick Ti_2C and Nb_2C revealed superior flexibility (observed by Foppl-von Karman number per unit area γ) and higher in-plane stiffness, compared to three-atom-thick MoS_2 (9.14 eV) [61]. Therefore, increasing the layer thickness decreases the flexibility of MXenes; however, better flexibility could be observed in MXenes with OH terminations, and the thinnest MXenes with a noticeable decrease in the in-plane stiffness (requires milder exfoliation techniques) [61]. As observed in Figure 8c, with increasing the layer thickness of MXenes, the in-plane stiffness, and out-of-plane bending rigidity increases [61]. Lastly, the bending rigidity increases with effective thickness t_s in a

cubic manner, as presented in Figure 8d where C/D ratios were plotted and γ and D considered as a function of effective thickness for 2D materials [61].

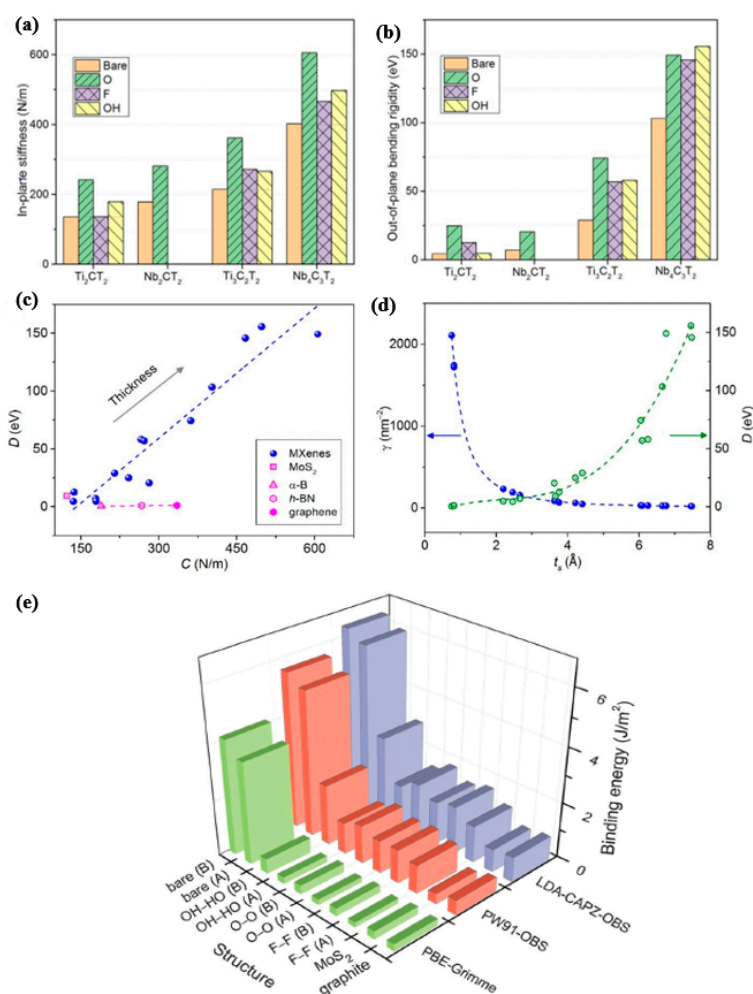


Figure 8. (a) In-plane stiffness and (b) out-of-plane bending rigidity MXenes. (c) Rigidity “D” vs. stiffness, (d) D vs. thickness t_s . Reproduced with permission from [61]. Copyright RSC, 2020. (e) Comparison of the theoretical binding energies of $Ti_3C_2T_2$, $T = OH, F,$ and O relative to different 2D materials. Reproduced with permission from [65]. Copyright RSC, 2016.

2.3. Interlayer Adhesion and Sliding

The interlayer adhesion energy and sliding resistance are two critical characteristics of MXenes that are affected by several parameters such as composition, shape, adhesion, and functional species. For instance, understanding the adhesion between MXenes and various substrates is crucial for MXene device fabrication and performance. DFT calculations demonstrated that the surface functionalities ($T = OH, F,$ and O) weaken interlayer coupling of $Ti_3C_2T_2$, relative to the bare counterparts as well as other different 2D materials (Figure 8e) [65]. The binding energies of stacked $Ti_{n+1}C_nT_2$ were found to be about 2- to 6-fold those of 2D graphite and MoS_2 materials with weak interlayer coupling. The interlayer coupling of $Ti_3C_2T_2$ depends on the surface functionalities, which decrease the interlayer coupling, resulting in exfoliation of the stacked $Ti_3C_2T_2$ into monolayers with outstanding mechanical properties compared to other 2D materials. The OH-containing functionalities were the most strongly coupled $Ti_3C_2T_2$ with the highest mechanical properties. The determined Young’s moduli normal to the layer plane was 226 GPa for Bernal- $Ti_3C_2(OH)_2$, which is more energetically preferred and also higher than that of highly oriented pyrolytic graphite (about 34 GPa). Furthermore, another study investigated the effect of surface functionalization on the sliding resistance of M_2CO_2 compared

to bare counterparts using DFT, along with exploring the strain effect on the sliding resistance [66]. At equilibrium, the layers can easily slide due to the smaller binding energy as a consequence of larger interlayer distance. Due to the oxygen hollow at the surface of oxygen functionalized MXenes, the sliding resistance is increased. However, due to the strong metallic interactions between the stacked M_2C layers, the sliding resistance is much higher than that of M_2CO_2 . Another finding is that the relation between the gap and the energy barrier is not linear, whereas as the strain increases, the gap first starts increasing until it reaches maximum value then starts decreasing again. Comparing different stacking configurations, the mirror stacked M_2CO_2 -II possesses a better lubricant property than the parallel stacked M_2CO_2 -I because its sliding energy barrier is much lower. In addition, the sliding barrier can be significantly enhanced by normal compression. Whereas, the interlayer sliding, owing to the transfer of different charges from M to O atom, may effectively be hindered by the in-plane biaxial tension. The minimum energy pathway can be modified entirely by the uniaxial tension strain due to anisotropic expansion of the surface electronic state. The functionalized MXenes with strain-controllable frictional properties promise lubricating materials due to their lower sliding resistance and superior mechanical properties.

Another study [67] investigated the effect of point defects on the friction coefficients using DFT calculations and classical MD simulations with reactive force-field (ReaxFF) potentials. The results revealed that the sliding pathways are with low energy barriers in all $Ti_{n+1}C_n$ ($n = 1, 2, \text{ and } 3$) systems. For these systems, both DFT and ReaxFF methods predicted friction coefficients for interlayer sliding, for normal loads below 1.2 GPa, to be between 0.24 and 0.273. It was found that titanium (Ti) vacancies in sublayers and terminal oxygen (O) vacancies at surfaces increased the friction coefficients, reaching almost 0.31. That is because the surface roughness increased, resulting in additional attractive forces between adjacent layers. Thereby, Ti_3C_2 with surfaces functionalized with $-OH$ and $-OCH_3$ groups were studied and found to be able to reduce the friction coefficient to 0.10 and 0.14, respectively.

Understanding of the adhesion among MXenes and different substrates is crucial for the fabrication of MXene devices. In this regard, the adhesion of $Ti_3C_2T_x$ and Ti_2CT_x with a SiO_2 -coated spherical Si tip was benchmarked compared to graphene (mono-, bi-, and tri-layer) and SiO_2 -coated Si tip substrate using direct AFM measurements [68]. This is based on using the Maugis-Dugdale theory for conversion of the adhesion force measured by the AFM to adhesion energy with consideration of the surface roughness [68]. The average adhesion energies of $Ti_3C_2T_x$ ($0.90 \pm 0.03 \text{ J m}^{-2}$) was higher than that of Ti_2CT_x ($0.40 \pm 0.02 \text{ J m}^{-2}$) and was in the range of adhesion between graphene and SiO_2 . The superior adhesion energy between SiO_2 and $Ti_3C_2T_x$ is due to its thicker monolayer relative to Ti_2CT_x . Another observation was that the adhesion energy of multilayer MXene stacks is dependent on the number of monolayers, in contrast to graphene, which is attributed to the larger interlayer spacing and monolayer thickness of the MXenes.

3. Self-Standing MXene as Electrode for Supercapacitors

Supercapacitors are highly efficient energy storage devices, owing to their excellent power density, fast charge propagation, and long-term durability. The capacitance performance can be calculated using the maximum stored energy (E) and this equation $E = 1/2 CV^2$, where C is the total capacitance, and V is the working voltage. Meanwhile, the power delivery (P) can be calculated using this equation $P = V^2/4R$, where R is the equivalent series resistance of the supercapacitor. Self-standing MXenes are among the most promising materials for supercapacitors due to their excellent electrical conductivity, mechanical flexibility, high surface area, and high capacitance [24,69,70]. Thereby, few reviews emphasized the utilization of MXenes as supercapacitors, which showed that self-standing $Ti_3C_2T_x$ is the most studied MXenes [71–73]. Several factors determine the capacitance performance of MXenes, such as their morphology, surface area, composition, preparation approaches, as well as the type of electrolytes. Table 2 shows the utilization of self-standing $Ti_3C_2T_x$ prepared by various approaches as efficient supercapacitors, which showed comparable or better performance than that of hybrid $Ti_3C_2T_x$ (i.e., combined with PPy, rGO, and CNTs) [74–76]. Table 3 shows the supercapacitance performance of

self-standing $\text{Ti}_3\text{C}_2\text{T}_x$ and hybrid $\text{Ti}_3\text{C}_2\text{T}_x$ in different electrolytes solutions. The performance of both self-standing and hybrid $\text{Ti}_3\text{C}_2\text{T}_x$ in acidic electrolytes (H_2SO_4) was significantly higher than that in alkaline or neutral electrolytes (Table 3). For example, $\text{Ti}_3\text{C}_2\text{T}_x$ showed capacitance performance of 70, 95, 245, and 450 F g^{-1} in KOH, MgSO_4 , 1 M H_2SO_4 , and 3 M H_2SO_4 , respectively [76–78]. The same phenomenon was observed in self-standing V_2CT_x , which showed the capacitance performance of (487 F g^{-1}) in H_2SO_4 compared to 225 F g^{-1} in MgSO_4 and 184 F g^{-1} in KOH [79]. Interestingly, the capacitance of self-standing V_2CT_x in H_2SO_4 electrolyte (487 F g^{-1}) [79] was superior to $\text{Ti}_3\text{C}_2\text{T}_x$, Mo_2CT_x , $\text{Mo}_{1.33}\text{CT}_x$ 245, 196, and 339 F g^{-1} , respectively [74,75,80]. The superior capacitance performance of self-standing MXenes in acidic electrolytes compared to in neutral or alkaline electrolytes is owing to the pseudocapacitive performance with surface redox reactions in acidic electrolytes relative to compared to the ion-intercalation capacitance in neutral and alkaline electrolytes [24]. The surface functionalities (i.e., O_2 , OH, and F) have a significant effect on the capacity of the H_2SO_4 electrolyte; The increase of O and decrease of F ions termination in $\text{Ti}_3\text{C}_2\text{T}_x$ increases the capacitance [81].

The pseudocapacitance characteristics and internal mechanism of various MXenes as supercapacitors deeply studied in H_2SO_4 electrolyte, in addition to the factors determine the capacitance effect via DFT calculations [81]. This is included various MXenes ($\text{M}_{n+1}\text{X}_n\text{T}_x$), where M = Sc, Ti, V, Zr, Nb, Mo; X = C, N; T = O, OH; n = 1–3) in H_2SO_4 electrolyte [82]. The predicted capacitance performance of $\text{Ti}_3\text{C}_2\text{T}_x$, Mo_2CT_x , and V_2CT_x [82,83] were similar to the experimentally measured capacitances 235, 245, 90, and 380 F g^{-1} , respectively [77,79,82].

Evaluating the descriptors for the capacitance trends, we find that more positive hydrogen adsorption free energy (weak binding to H) and smaller change of the potential at the point of zero charge after H binding lead to higher capacitance. Interestingly, the pseudocapacitive performance of nitride MXenes electrodes outperformed carbide MXenes. Mainly, Ti_2NT_x is expected to possess a high gravimetric capacitance under any applied voltage in H_2SO_4 , owing to the low atomic weight and favorable redox chemistry of Ti. Meanwhile, $\text{Zr}_{n+1}\text{N}_n\text{T}_x$ is anticipated to possess the best areal capacitive performance [82]. The higher capacitance performance is attributed to the higher adsorption free energy and lower change of the potential at the point of zero charge after H binding [82]. The relationship between the charge storage of nitride and carbide MXenes against the shift in the point-of-zero-charge (V_{PZC}) and H_2 adsorption free energy (ΔG_{H}) displayed that the large ΔGH and the low Δp_{zC} lead to higher charge storage per unit of formula (Figure 9) [82]. Thereby, Zr-based nitride MXenes (Zr_2N , Zr_3N_2 , and Zr_4N_3) reveal the highest charge storage under an applied potential range from -1 to 1 V vs. standard Hydrogen Electrode (SHE) [82].

Although the tremendous progress in the capacitance performance MXenes, some remaining gaps exist among the theoretical calculations and experiments, such as inaccurate consideration of the multilayered structures of MXenes along with ignoring the F-rich MXenes surface [84,85].

Table 2. Freestanding $Ti_3C_2T_x$ MXenes prepared by various approaches as efficient supercapacitors compared to some $Ti_3C_2T_x$ composites as a function of preparation method. Abbreviations: PPy = polypyrrole, rGO = reduced graphene oxide, CNT = carbon nanotubes and EG = electrochemically exfoliated graphene.

MAX Phase MXene-Hybrid	Material Composition	Synthesis/Characterization Methods	Morphology	Performance	Ref.
Ti_3AlC_2	$Ti_3C_2T_x$	HF etching/TEM, SEM, CA, XRD, EIS	Nanosheets	517 F/g at 1 A/g	[16]
Ti_3AlC_2	$Ti_3C_2T_x$	HF etching/EIS, XRD	Paper	340 F/cm ³ at 1 A/g	[76]
Ti_3AlC_2	$Ti_3C_2T_x$ -P	HCl-LiF/SEM, TEM, FTIR	Paper	416 F/g at 5 mV/s	[84]
Ti_3AlC_2	$Ti_3C_2T_x$	HCl-LiF/XRD, TEM, SEM	Nanosheets	900 F/cm ³ at 2 mV/s	[77]
Ti_3AlC_2	$Ti_3C_2T_x$ -EG	HF etching/XRD, TEM, SEM	Nanosheets	33 F/cm ² at 2 mV/s	[86]
Ti_3AlC_2	$Ti_3C_2T_x$	HF etching/NA	Film	528 F/cm ³ at 2 mV/s	[87]
Ti_3AlC_2	$Ti_3C_2T_x$	NH ₄ F-hydrothermal/XRD, SEM, Raman, XPS	Nanosheets	141 F/g at 2 A/g	[88]
Ti_3AlC_2	$Ti_3C_2T_x$ -rGO	HCl-LiF/XRD, SEM	Nanosheets	8.6 mWh/cm ³ at 0.2 W/cm ³	[89]
Ti_3AlC_2	$Ti_3C_2T_x$ -CNT	HCl-LiF/XRD, SEM, TEM	Nanosheets	314 F/cm ³ at 1.7 mg/cm ²	[90]
Ti_3AlC_2	$Ti_3C_2T_x$	HF etching/NA	Nanosheets	2.8 mWh/cm ³ at 0.225 W/cm ³	[91]
Ti_3AlC_2	BiOCl-Ti ₃ C ₂ T _x	HF etching/XRD, SEM, TEM, XPS	Nanosheets	397 F/cm ³ at 1 A/g	[92]
Ti_3AlCN	$Ti_3C_2T_x$	HCl-LiF/TEM, AFM, SEM	Nanosheets	61 mF/cm ² at 5 μA/cm ²	[93]

Table 3. Freestanding $Ti_3C_2T_x$ and Ti_2CT_x MXenes supercapacitors compared to some $Ti_3C_2T_x$ composites as a function of electrolyte and scan rate/current density. Abbreviations: PPy = polypyrrole, rGO = reduced graphene oxide, CNT = carbon nanotubes, PVA = polyvinyl alcohol, and SWCNT = single-walled carbon nanotubes.

Freestanding $Ti_3C_2T_x$ and Ti_2CT_x MXenes						
Electrode	Electrolyte	Scan Rate/Current Density	Initial Capacitance (IC)	Cycle Number (CN)	Capacity After Cycles (AC)	Ref.
Ti_2CT_x	30 wt % KOH	10 A g ⁻¹	51 F g ⁻¹	6000	93%	[74]
$Ti_3C_2T_x$	1 M KOH	1 A g ⁻¹	350 F cm ⁻³	10,000	~94%	[76]
$Ti_3C_2T_x$	1 M H ₂ SO ₄	5 A g ⁻¹	415 F cm ⁻³	10,000	~100%	[81]
$Ti_3C_2T_x$	1 M H ₂ SO ₄	10 A g ⁻¹	900 F cm ⁻³	10,000	~100%	[77]
$Ti_3C_2T_x$	1 M H ₂ SO ₄	10 A g ⁻¹	499 F g ⁻¹	10,000	~100%	[94]
$Ti_3C_2T_x$	6 M KOH	5 A g ⁻¹	118 F g ⁻¹	5000	~100%	[95]
$Ti_3C_2T_x$	1 M H ₂ SO ₄	5 A g ⁻¹	215 F g ⁻¹	10,000	~100%	[96]
$Ti_3C_2T_x$	1 M H ₂ SO ₄	5 A g ⁻¹	892 F g ⁻¹	10,000	~100%	[97]
N- $Ti_3C_2T_x$	1 M H ₂ SO ₄	50 mV s ⁻¹	192 F g ⁻¹	10,000	92%	[98]
$Ti_3C_2T_x$ /paper	1 M H ₂ SO ₄	2 mA cm ⁻²	25 mF cm ⁻²	10,000	92%	[99]
$Ti_3C_2T_x$ /3D porous layered double hydroxide	6 M KOH	1 A g ⁻¹	1061 F g ⁻¹	4000	70%	[100]
400-KOH- $Ti_3C_2T_x$	1 M H ₂ SO ₄	1 A g ⁻¹	517 F g ⁻¹	10,000	>99%	[101]
$Ti_3C_2T_x$ MXenes Hybrid Composites						
Electrode	Electrolyte	Scan Rate/Current Density	Initial Capacitance (IC)	Cycle Number (CN)	Capacity After Cycles (AC)	Ref.
$Ti_3C_2T_x$ /PVA	1 M KOH	5 A g ⁻¹	~370 F cm ⁻³	10,000	~85%	[16]
PPy/ $Ti_3C_2T_x$	1 M H ₂ SO ₄	100 mV s ⁻¹	~250 F g ⁻¹	25,000	92%	[84]
$Ti_3C_2T_x$ /SWCNT	1 M MgSO ₄	5 A g ⁻¹	345 F cm ⁻³	10,000	~100%	[102]
$Ti_3C_2T_x$ /rGO	3 M H ₂ SO ₄	100 mV s ⁻¹	777 F cm ⁻³	20,000	~100%	[103]
$Ti_3C_2T_x$ /CNT	1 M EMITFSI	1 A g ⁻¹	~80 F g ⁻¹	1000	~90%	[104]
$Ti_3C_2T_x$ /CNT	6 M KOH	10 mV s ⁻¹	~384 F g ⁻¹	10,000	~100%	[105]
TiO ₂ / $Ti_3C_2T_x$	6 M KOH	5 mV s ⁻¹	143 F g ⁻¹	3000	~96%	[106]
MnO _x / $Ti_3C_2T_x$	1 M Li ₂ SO ₄	2 mV s ⁻¹	602 F cm ⁻³	10,000	89.8%	[107]
PPy/ $Ti_3C_2T_x$	0.5 M H ₂ SO ₄	1 mA cm ⁻²	406 F cm ⁻³	20,000	~96%	[108]

Increasing the specific surface areas (SSA) and the active redox sites of MXenes can enhance their capacitance performance. Using these strategies, the capacitances of macroporous $\text{Ti}_3\text{C}_2\text{T}_x$ and $\text{Ti}_3\text{C}_2\text{T}_x$ hydrogels reached 210 and 380 F g^{-1} , respectively, owing to their abundance of active sites resulted from the high SSA [84,109]. Moreover, macroporous $\text{Ti}_3\text{C}_2\text{T}_x$ shows capacitances of 310 , 210 , and 100 F g^{-1} at scan rates of 0.01 , 10 , and 40 V s^{-1} , respectively [78]. This indicated the direct correlation between the current density peak (i) current and scan rate (v), which can be an indicator for the inherent charge storage kinetics as can be calculated using this equation $i = av^b$, where a and b are constants. Electrodes of supercapacitors usually possess a linear relationship between v and i , i.e., $(i \sim v)$.

To this end, macroporous $\text{Ti}_3\text{C}_2\text{T}_x$ in H_2SO_4 electrolyte showed a pseudocapacitive behavior as found in the linear dependence of $\log i$ vs. $\log v$, i.e., $b \approx 1$ [78].

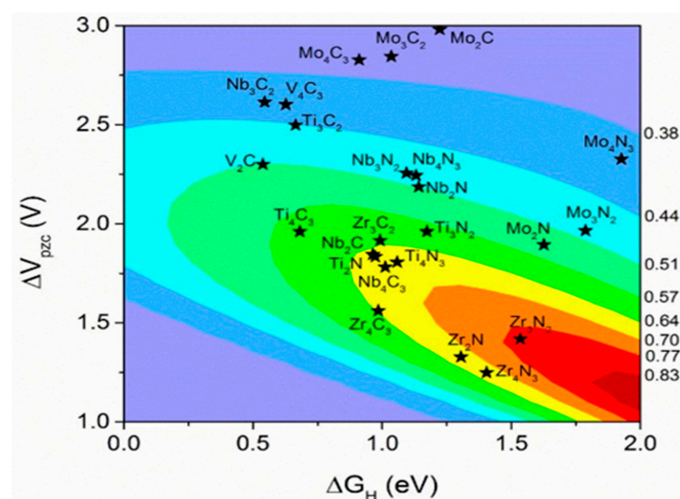


Figure 9. Color map of the relationship between the charge storage per formula unit against the shift in the V_{PZC} and H_2 adsorption free energy (ΔG_H). The applied potential ranged from -1 to 1 V vs. standard Hydrogen Electrode (SHE). Reproduced with permission from [82]. Copyright ACS, 2019.

Another factor for improvement of the capacitance performance of MXenes is the selection of appropriate electrolyte, due to the difference in the ionic conductivity, operation voltage, the temperature of different electrolytes that subsequently tailor the capacitance performance. Thereby, aqueous electrolytes with their outstanding ionic conductivity are preferred compared to organic or ionic liquids electrolytes, although the ionic liquids electrolytes have the largest potential window and feasible for high working temperatures. This finding was achieved in the superior capacitance of $\text{Ti}_3\text{C}_2\text{T}_x$ (325 F g^{-1}) in H_2SO_4 [81], compared to (70 F g^{-1}) in ionic liquid electrolytes [110] and (32 F g^{-1}) in organic electrolytes [104]. The capacitance performance of $\text{Ti}_3\text{C}_2\text{T}_x$ in propylene carbonate (PC) organic electrolyte with higher ionic conductivity was higher than that in acetonitrile and dimethyl sulfoxide (DMSO), with lower ionic conductivity [111]. The preparation method of MXenes is also an essential factor for boosting the mechanical properties and electrochemical or capacitance performance. Investigation of the mechanical evolution during the intercalation/deintercalation of MXenes revealed that Li-ion intercalation increases the out-of-plane stiffness (elastic properties) in aqueous electrolytes [59]. This is achieved by proposing a theoretical correlation among the cation content and the out-of-plane elastic properties during electrochemical reactions.

Although MXenes were reported to be promising for energy storage applications, their restacking issue, low intrinsic electronic and ionic conductivity, and low specific capacity hinder their use in the practical applications [24]. Besides, the underlying mechanism of the use of MXenes for supercapacitors still needs to be clarified, and that requires further in-depth theoretical and experimental investigations. Furthermore, due to the remarkable influence of the electrolytes on the MXene supercapacitors, more studies are needed for electrolytes optimization.

4. Mechanical of Self-Standing MXenes vs. Hybrid MXenes

MXenes, especially $\text{Ti}_3\text{C}_2\text{T}_x$, was found to be a promising candidate for enhancing the mechanical properties of various polymers, metals, and carbon materials. This is owing to the multilayered 2D structure and outstanding Young's modulus of $\text{Ti}_3\text{C}_2\text{T}_x$ monolayer (0.33 ± 0.03 TPa), measured via the nanoindentation experiments [2]. For instance, the mechanical properties of polyvinyl alcohol (PVA) nanofibers were significantly enhanced via using $\text{Ti}_3\text{C}_2\text{T}_x$ and cellulose nanocrystals (CNC) fillers (denoted as PVA/CNC/ $\text{Ti}_3\text{C}_2\text{T}_x$) compared to pristine PVA [112]. Notably, PVA nanofibers containing 0.07 wt.% of both CNC and $\text{Ti}_3\text{C}_2\text{T}_x$ displayed more than 100% enhancement of the storage modulus relative to PVA nanofibers. In comparison, PVA nanofibers with 3 wt.% nanocellulose (PVA/CNC) revealed a 74% increase in storage modulus of PVA at 25 °C [112]. Additionally, the elastic modulus of PVA/CNC/ $\text{Ti}_3\text{C}_2\text{T}_x$ nanofibers (855 MPa) was 2.1 times higher than that of PVA nanofibers (392 MPa). The Young's modulus of PVA/CNC/ $\text{Ti}_3\text{C}_2\text{T}_x$ nanofibers (293 ± 59 MPa.) was higher than that of PVA/CNC (241 ± 51 MPa), PVA/ $\text{Ti}_3\text{C}_2\text{T}_x$ (283 ± 60 MPa), and PVA nanofibers (221 ± 51 MPa) [112]. Likewise, polyimide/ $\text{Ti}_3\text{C}_2\text{T}_x$ aerogel prepared via the freeze-drying of and annealing to form a robust, lightweight, and hydrophobic aerogel (Figure 10a) with three-dimensional “house of cards” structure (Figure 10b) [113]. The compressive strength at 80% strain and Young's modulus of elasticity for PI/ $\text{Ti}_3\text{C}_2\text{T}_x$ aerogel increased significantly with decreasing the $\text{Ti}_3\text{C}_2\text{T}_x$ concentration. This is owing to greater porosity and lower density of PI/MXene aerogels with the increase of the $\text{Ti}_3\text{C}_2\text{T}_x$ amount [113]. Interestingly, the elastic properties, PI/MXene-3 with a ratio of 5.2:1, respectively, showed impressive stress–strain repeatability after 50 cycles of compression-release (Figure 10c), attributed to the strong interactions between PI chains and $\text{Ti}_3\text{C}_2\text{T}_x$ nanosheets in the hybrid aerogel [113]. Silver nanowires, combined with $\text{Ti}_3\text{C}_2\text{T}_x$ (AgNWs- $\text{Ti}_3\text{C}_2\text{T}_x$) transparent conductive electrode, displayed a higher conductivity, chemical stability, and mechanical stability than that of pristine AgNW electrode [114].

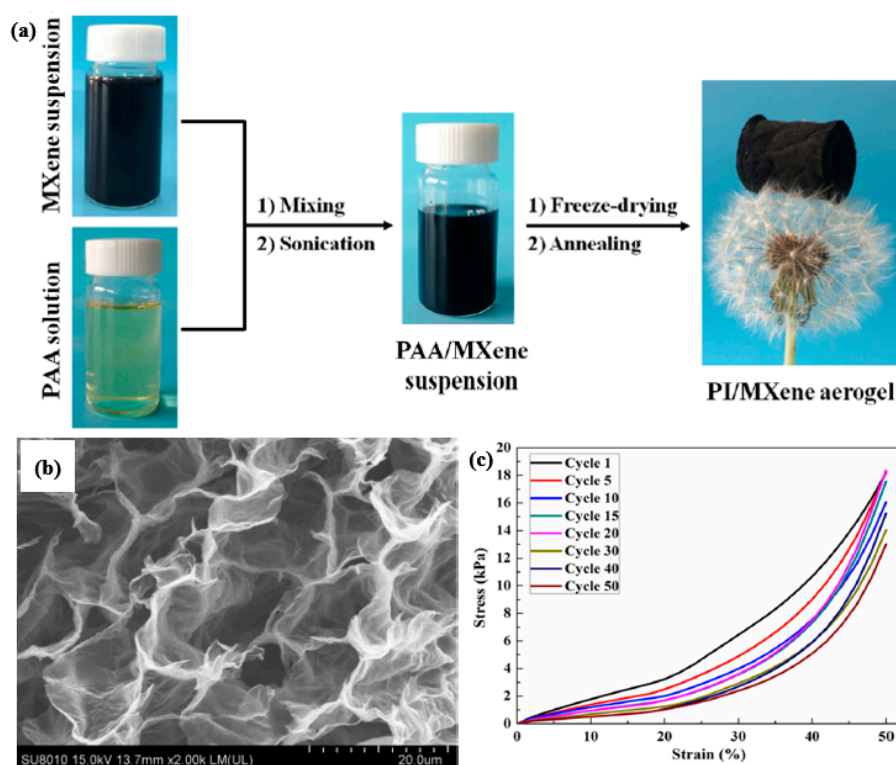


Figure 10. (a) Preparation route of PI/ $\text{Ti}_3\text{C}_2\text{T}_x$ aerogels (b) Internal structure of PI/ $\text{Ti}_3\text{C}_2\text{T}_x$ -3 aerogels (c) Stress–strain curves for 50 repeated compression cycles on the PI/MXene-3 aerogel at 50% strain. Adapted and reproduced with permission from [113]. Copyright ACS, 2019.

$\text{Ti}_3\text{C}_2\text{T}_x$ /carbon nanotube (CNT) 3D porous aerogel (denoted as MXCNT) was synthesized using the bidirectional freezing approach (Figure 11a) [115]. Figure 11b displays the compressive stress-strain curves for $\text{Ti}_3\text{C}_2\text{T}_x$ and MXCNT aerogels measured under compression at a displacement rate of 1 mm/min up to 50% strain. The compressive strength of MXCNT was substantially higher than that of $\text{Ti}_3\text{C}_2\text{T}_x$ (Figure 11b). Also, the compressive strength of MXCNT increased with increasing CNT concentration to reach the maximum value of 25,000 Pa using a ratio of 1/3 of $\text{Ti}_3\text{C}_2\text{T}_x$ /CNT, respectively. This is originated from the uniform distribution of $\text{Ti}_3\text{C}_2\text{T}_x$ multilayered sheets with CNT in the direction of the compressive force resulting in a uniform aerogel, as shown in (Figure 11c). Interestingly, the as-formed MXCNT aerogel can afford more than 500 times (Figure 11d) and more than 2100 times (Figure 11e) of its weight without collapsing along with recovery of 12.1 % strain after eliminating the applied load. The significant enhancement in the compressive strength of MXCNT is ascribed to the ordered porous framework supported by vertical pillars, that warrants the cell walls deformation on compression rather than sliding between the walls [115]. The MXCNT aerogel is highly promising for electromagnetic interference (EMI) shielding applications.

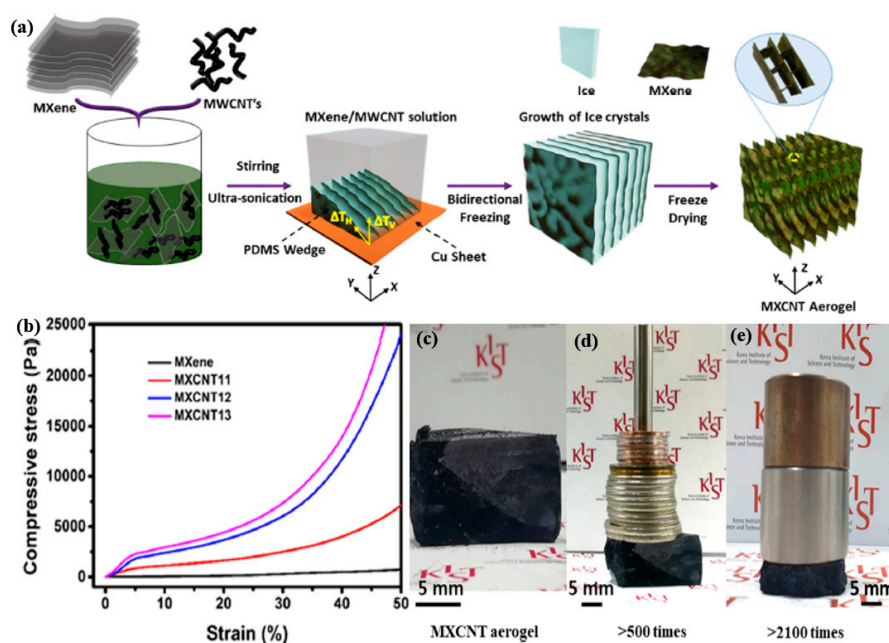


Figure 11. (a) Preparation of MXene/CNT hybrid aerogels through bidirectional freezing approach (b) Stress-strain curves of pristine MXene aerogels and MXene/CNT hybrid aerogels samples (c–e) MXene/CNT hybrid aerogels supporting more than >500 and >2100 times of its weight with no obvious collapsing. Adapted and reproduced with permission from [115]. Copyright ACS, 2019.

5. Summary and Perspectives

In summary, this review emphasized the recent advances in the mechanical properties of self-standing MXenes, including elastic properties, bending rigidity, and adhesion and sliding resistance from the experimental and theoretical views. This is, besides, to compare the mechanical properties of self-standing MXenes with hybrid MXenes along with their utilization as supercapacitors. Both experimental and theoretical calculations implied the significant effect of shape (i.e., layer thickness, interlayer spacing, dimensional, and porosity), preparation method, type (i.e., carbides or nitrides), composition (i.e., mono-/binary/multi-metals, doping, defects, and decoration with nanoparticles or single atoms), and functional groups (O, OH, and F) on enhancement the mechanical properties of MXenes. These features endowed the mechanical properties of MXenes are found to be closer to various 2D materials such as graphene, molybdenum disulfide, and boronitrene.

Despite the significant progress achieved in the rational design of self-standing MXenes, their mechanical properties are frequently investigated theoretically rather than experimentally. Additionally, the preparation approaches of MXenes entail multiple complicated steps, hazard chemicals, and without precise monitoring, shape, composition, and surface/bulk functionalities. However, the theoretical calculations predicted the synthesis of dozens of MXenes with outstanding mechanical merits coupled with electrical conductivity, high surface area, and ion adsorption/storage properties, which leaves extensive gates for the utilization of MXenes in various applications such as flexible devices, energy production/storage devices, and sensors. To this end, the capacitance performances of MXenes were enhanced significantly via their integration with conductive polymers, carbon-based materials (i.e., graphene, carbon nanotubes), and doping or functionalization metals (i.e., transition metals, noble metals, non-metals traces, semiconductors). Thereby, the mechanical properties of self-standing MXenes and their mechanism should be highlighted experimentally rather than through theoretically. Also, the combination between MXenes and other carbon-based materials and novel metallic nano architectonics can lead to impressive properties and applications [116–119]. Thus, the presented review can provide a guided roadmap for the scientists to design novel MXenes for the coming generations of energy conversion and storage devices as well as smart sensors.

Author Contributions: All authors contributed equally to this work. Collecting the data and writing-original draft preparation, Y.I. and A.M. contributed equally; writing-review and editing, K.E.; review editing, A.M.A. (Ahmed M. Abdelgawad), supervision and project administration, A.M.A. (Aboubakr M. Abdullah) and A.E. All authors have read and agreed to the published version of the manuscript.

Funding: This publication was supported by Qatar University, internal grant number QUHI-CAS-19/20-1. The findings achieved herein are solely the responsibility of the authors.

Acknowledgments: The authors gratefully thank Hydro and Qatar Aluminium Limited (QSC).

Conflicts of Interest: The authors declare no conflict of interest.

References

1. Liu, M.; Zhang, R.; Chen, W. Graphene-supported nanoelectrocatalysts for fuel cells: Synthesis, properties, and applications. *Chem. Rev.* **2014**, *114*, 5117–5160. [[CrossRef](#)] [[PubMed](#)]
2. Lipatov, A.; Lu, H.; Alhabeib, M.; Anasori, B.; Gruverman, A.; Gogotsi, Y.; Sinitskii, A. Elastic properties of 2D Ti₃C₂T_x MXene monolayers and bilayers. *Sci. Adv.* **2018**, *4*, eaat0491. [[CrossRef](#)] [[PubMed](#)]
3. Eid, K.; Sliem, M.H.; Al-Kandari, H.; Sharaf, M.A.; Abdullah, A.M. Rational synthesis of porous graphitic-like carbon nitride nanotubes codoped with Au and Pd as an efficient catalyst for carbon monoxide oxidation. *Langmuir* **2019**, *35*, 3421–3431. [[CrossRef](#)] [[PubMed](#)]
4. Eid, K.; Sliem, M.H.; Abdullah, A.M. Unraveling template-free fabrication of carbon nitride nanorods codoped with Pt and Pd for efficient electrochemical and photoelectrochemical carbon monoxide oxidation at room temperature. *Nanoscale* **2019**, *11*, 11755–11764. [[CrossRef](#)] [[PubMed](#)]
5. Abdu, H.I.; Eid, K.; Abdullah, A.M.; Han, Z.; Ibrahim, M.H.; Shan, D.; Chen, J.; Elzatahry, A.A.; Lu, X. Unveiling one-pot scalable fabrication of reusable carboxylated heterogeneous carbon-based catalysts from eucalyptus plant with the assistance of dry ice for selective hydrolysis of eucalyptus biomass. *Renew. Energy* **2020**, *153*, 998–1004. [[CrossRef](#)]
6. Anasori, B.; Gogotsi, Y. *2D Metal Carbides and Nitrides (MXenes): Structure, Properties and Applications*; Springer International Publishing: Berlin/Heidelberg, Germany, 2019; p. 534. [[CrossRef](#)]
7. Idris Abdu, H.; Eid, K.; Abdullah, A.M.; Sliem, M.H.; Elzatahry, A.; Lu, X. Dry ice-mediated rational synthesis of edge-carboxylated crumpled graphene nanosheets for selective and prompt hydrolysis of cellulose and eucalyptus lignocellulose under ambient reaction conditions. *Green Chem.* **2020**, *22*, 5437–5446. [[CrossRef](#)]
8. Deysher, G.; Shuck, C.E.; Hantanasirisakul, K.; Frey, N.C.; Foucher, A.C.; Maleski, K.; Sarycheva, A.; Shenoy, V.B.; Stach, E.A.; Anasori, B.; et al. Synthesis of Mo₄VAIC₄ MAX Phase and Two-Dimensional Mo₄VC₄ MXene with Five Atomic Layers of Transition Metals. *ACS Nano* **2020**, *14*, 204–217. [[CrossRef](#)]
9. Jun, B.M.; Her, N.; Park, C.M.; Yoon, Y. Effective removal of Pb(II) from synthetic wastewater using Ti₃C₂T_x MXene. *Environ. Sci. Water Res. Technol.* **2020**, *6*, 173–180. [[CrossRef](#)]

10. Han, M.; Shuck, C.E.; Rakhmanov, R.; Parchment, D.; Anasori, B.; Koo, C.M.; Friedman, G.; Gogotsi, Y. Beyond Ti_3C_2Tx : MXenes for Electromagnetic Interference Shielding. *ACS Nano* **2020**, *14*, 5008–5016. [[CrossRef](#)]
11. Amiri, A.; Chen, Y.; Bee Teng, C.; Naraghi, M. Porous nitrogen-doped MXene-based electrodes for capacitive deionization. *Energy Storage Mater.* **2020**, *25*, 731–739. [[CrossRef](#)]
12. Rasool, K.; Pandey, R.P.; Rasheed, P.A.; Buczek, S.; Gogotsi, Y.; Mahmoud, K.A. Water treatment and environmental remediation applications of two-dimensional metal carbides (MXenes). *Mater. Today* **2019**, *30*, 80–102. [[CrossRef](#)]
13. Ibrahim, Y.; Kassab, A.; Eid, K.; Abdullah, A.M.; Ozoemena, K.I.; Elzatahry, A. Unveiling Fabrication and Environmental Remediation of MXene-Based Nanoarchitectures in Toxic Metals Removal from Wastewater: Strategy and Mechanism. *Nanomaterials* **2020**, *10*, 885. [[CrossRef](#)] [[PubMed](#)]
14. Barsoum, M.; El-Raghy, T. The MAX phases: Unique new carbide and nitride materials ternary ceramics turn out to be surprisingly soft and machinable, yet also heat-tolerant, strong and lightweight. *Am. Sci.* **2001**, *89*, 334–343. [[CrossRef](#)]
15. Barsoum, M.W.; Radovic, M. Elastic and Mechanical Properties of the MAX Phases. *Annu. Rev. Mater. Res.* **2011**, *41*, 195–227. [[CrossRef](#)]
16. Ling, Z.; Ren, C.E.; Zhao, M.-Q.; Yang, J.; Giammarco, J.M.; Qiu, J.; Barsoum, M.W.; Gogotsi, Y. Flexible and conductive MXene films and nanocomposites with high capacitance. *Proc. Natl. Acad. Sci. USA* **2014**, *111*, 16676. [[CrossRef](#)] [[PubMed](#)]
17. Zhan, X.; Si, C.; Zhou, J.; Sun, Z. MXene and MXene-based composites: Synthesis, properties and environment-related applications. *Nanoscale Horiz.* **2020**, *5*, 235–258. [[CrossRef](#)]
18. Li, Y.; Wang, J.; Liu, X.; Zhang, S. Towards a molecular understanding of cellulose dissolution in ionic liquids: Anion/cation effect, synergistic mechanism and physicochemical aspects. *Chem. Sci.* **2018**, *9*, 4027–4043. [[CrossRef](#)] [[PubMed](#)]
19. Chen, J.; Huang, Q.; Huang, H.; Mao, L.; Liu, M.; Zhang, X.; Wei, Y. Recent progress and advances in the environmental applications of MXene related materials. *Nanoscale* **2020**, *12*, 3574–3592. [[CrossRef](#)]
20. Li, J.; Li, X.; Van der Bruggen, B. An MXene-based membrane for molecular separation. *Environ. Sci. Nano* **2020**. [[CrossRef](#)]
21. Zhao, P.; Jian, M.; Zhang, Q.; Xu, R.; Liu, R.; Zhang, X.; Liu, H. A new paradigm of ultrathin 2D nanomaterial adsorbents in aqueous media: Graphene and GO, MoS_2 , MXenes, and 2D MOFs. *J. Mater. Chem. A* **2019**, *7*, 16598–16621. [[CrossRef](#)]
22. Yang, B.; She, Y.; Zhang, C.; Kang, S.; Zhou, J.; Hu, W. Nitrogen Doped Intercalation $TiO_2/TiN/Ti_3C_2Tx$ Nanocomposite Electrodes with Enhanced Pseudocapacitance. *Nanomaterials* **2020**, *10*, 345. [[CrossRef](#)]
23. Yao, Z.; Sun, H.; Sui, H.; Liu, X. Construction of BPQDs/ $Ti_3C_2@TiO_2$ Composites with Favorable Charge Transfer Channels for Enhanced Photocatalytic Activity under Visible Light Irradiation. *Nanomaterials* **2020**, *10*, 452. [[CrossRef](#)]
24. Fu, Z.; Wang, N.; Legut, D.; Si, C.; Zhang, Q.; Du, S.; Germann, T.C.; Francisco, J.S.; Zhang, R. Rational Design of Flexible Two-Dimensional MXenes with Multiple Functionalities. *Chem. Rev.* **2019**, *119*, 11980–12031. [[CrossRef](#)] [[PubMed](#)]
25. Anasori, B.; Lukatskaya, M.R.; Gogotsi, Y. 2D metal carbides and nitrides (MXenes) for energy storage. *Nat. Rev. Mater.* **2017**, *2*, 16098. [[CrossRef](#)]
26. Kumar, K.S.; Choudhary, N.; Jung, Y.; Thomas, J. Recent Advances in Two-Dimensional Nanomaterials for Supercapacitor Electrode Applications. *ACS Energy Lett.* **2018**, *3*, 482–495. [[CrossRef](#)]
27. Zha, X.H.; Luo, K.; Li, Q.; Huang, Q.; He, J.; Wen, X.; Du, S. Role of the surface effect on the structural, electronic and mechanical properties of the carbide MXenes. *EPL* **2015**, *111*, 26007. [[CrossRef](#)]
28. Fu, Z.; Zhang, S.; Legut, D.; Germann, T.C.; Si, C.; Du, S.; Francisco, J.S.; Zhang, R. A synergetic stabilization and strengthening strategy for two-dimensional ordered hybrid transition metal carbides. *Phys. Chem. Chem. Phys.* **2018**, *20*, 29684–29692. [[CrossRef](#)]
29. Yorulmaz, U.; Özden, A.; Perkgöz, N.K.; Ay, F.; Sevik, C. Vibrational and mechanical properties of single layer MXene structures: A first-principles investigation. *Nanotechnology* **2016**, *27*, 335702. [[CrossRef](#)]
30. Zhang, H.; Fu, Z.; Zhang, R.; Zhang, Q.; Tian, H.; Legut, D.; Germann, T.C.; Guo, Y.; Du, S.; Francisco, J.S. Designing flexible 2D transition metal carbides with strain-controllable lithium storage. *Proc. Natl. Acad. Sci. USA* **2017**, *114*, E11082–E11091. [[CrossRef](#)]

31. Si, C.; Duan, W.; Liu, Z.; Liu, F. Electronic strengthening of graphene by charge doping. *Phys. Rev. Lett.* **2012**, *109*, 226802. [[CrossRef](#)]
32. Plummer, G.; Anasori, B.; Gogotsi, Y.; Tucker, G.J. Nanoindentation of monolayer $Ti_{n+1}C_nT_x$ MXenes via atomistic simulations: The role of composition and defects on strength. *Comput. Mater. Sci.* **2019**, *157*, 168–174. [[CrossRef](#)]
33. Zhang, L.; Yu, J.; Yang, M.; Xie, Q.; Peng, H.; Liu, Z. Janus graphene from asymmetric two-dimensional chemistry. *Nat. Commun.* **2013**, *4*, 1443. [[CrossRef](#)] [[PubMed](#)]
34. Zha, X.-H.; Yin, J.; Zhou, Y.; Huang, Q.; Luo, K.; Lang, J.; Francisco, J.S.; He, J.; Du, S. Intrinsic Structural, Electrical, Thermal, and Mechanical Properties of the Promising Conductor Mo_2C MXene. *J. Phys. Chem. C* **2016**, *120*, 15082–15088. [[CrossRef](#)]
35. Peng, Q.; De, S. Outstanding mechanical properties of monolayer MoS_2 and its application in elastic energy storage. *Phys. Chem. Chem. Phys.* **2013**, *15*, 19427–19437. [[CrossRef](#)] [[PubMed](#)]
36. Wu, D.; Wang, S.; Yuan, J.; Yang, B.; Chen, H. Modulation of the electronic and mechanical properties of phagraphene via hydrogenation and fluorination. *Phys. Chem. Chem. Phys.* **2017**, *19*, 11771–11777. [[CrossRef](#)]
37. Guo, Z.; Zhou, J.; Si, C.; Sun, Z. Flexible two-dimensional $Ti_{n+1}C_n$ ($n = 1, 2$ and 3) and their functionalized MXenes predicted by density functional theories. *Phys. Chem. Chem. Phys.* **2015**, *17*, 15348–15354. [[CrossRef](#)] [[PubMed](#)]
38. Zhou, J.; Zha, X.; Chen, F.Y.; Ye, Q.; Eklund, P.; Du, S.; Huang, Q. A Two-Dimensional Zirconium Carbide by Selective Etching of Al_3C_3 from Nanolaminated $Zr_3Al_3C_5$. *Angew. Chem. Int. Ed.* **2016**, *55*, 5008–5013. [[CrossRef](#)] [[PubMed](#)]
39. Fu, Z.H.; Zhang, Q.F.; Legut, D.; Si, C.; Germann, T.C.; Lookman, T.; Du, S.Y.; Francisco, J.S.; Zhang, R.F. Stabilization and strengthening effects of functional groups in two-dimensional titanium carbide. *Phys. Rev. B* **2016**, *94*, 104103. [[CrossRef](#)]
40. Bai, Y.; Zhou, K.; Srikanth, N.; Pang, J.H.L.; He, X.; Wang, R. Dependence of elastic and optical properties on surface terminated groups in two-dimensional MXene monolayers: A first-principles study. *RSC Adv.* **2016**, *6*, 35731–35739. [[CrossRef](#)]
41. Kurtoglu, M.; Naguib, M.; Gogotsi, Y.; Barsoum, M. First Principles Study of Two-dimensional Early Transition Metal Carbides. *MRS Commun.* **2012**, *2*. [[CrossRef](#)]
42. Borysiuk, V.N.; Mochalin, V.N.; Gogotsi, Y. Molecular dynamic study of the mechanical properties of two-dimensional titanium carbides $Ti_{n+1}C_n$ (MXenes). *Nanotechnology* **2015**, *26*, 265705. [[CrossRef](#)] [[PubMed](#)]
43. Lee, C.; Wei, X.; Kysar, J.W.; Hone, J. Measurement of the Elastic Properties and Intrinsic Strength of Monolayer Graphene. *Science* **2008**, *321*, 385–388. [[CrossRef](#)] [[PubMed](#)]
44. Jin, W.; Wu, S.; Wang, Z. Structural, electronic and mechanical properties of two-dimensional Janus transition metal carbides and nitrides. *Phys. E Low Dimens. Syst. Nanostruct.* **2018**, *103*, 307–313. [[CrossRef](#)]
45. Khazaei, M.; Ranjbar, A.; Arai, M.; Sasaki, T.; Yunoki, S. Electronic properties and applications of MXenes: A theoretical review. *J. Mater. Chem. C* **2017**, *5*, 2488–2503. [[CrossRef](#)]
46. Çakır, D.; Peeters, F.M.; Sevik, C. Mechanical and thermal properties of h - MX_2 ($M = Cr, Mo, W$; $X = O, S, Se, Te$) monolayers: A comparative study. *Appl. Phys. Lett.* **2014**, *41*, 10891–10896. [[CrossRef](#)]
47. Duerloo, K.A.N.; Ong, M.T.; Reed, E.J. Intrinsic Piezoelectricity in Two-Dimensional Materials. *J. Phys. Chem. Lett.* **2012**, *3*, 2871–2876. [[CrossRef](#)]
48. Zhou, J.; Zha, X.; Zhou, X.; Chen, F.; Gao, G.; Wang, S.; Shen, C.; Chen, T.; Zhi, C.; Eklund, P.; et al. Synthesis and Electrochemical Properties of Two-Dimensional Hafnium Carbide. *ACS Nano* **2017**, *11*, 3841–3850. [[CrossRef](#)]
49. Holm, A.; Park, J.; Goodman, E.D.; Zhang, J.; Sinclair, R.; Cargnello, M.; Frank, C.W. Synthesis, Characterization, and Light-Induced Spatial Charge Separation in Janus Graphene Oxide. *Chem. Mater.* **2018**, *30*, 2084–2092. [[CrossRef](#)]
50. Xu, C.; Wang, L.; Liu, Z.; Chen, L.; Guo, J.; Kang, N.; Ma, X.-L.; Cheng, H.-M.; Ren, W. Large-area high-quality 2D ultrathin Mo_2C superconducting crystals. *Nat. Mater.* **2015**, *14*, 1135–1141. [[CrossRef](#)]
51. Chakraborty, P.; Das, T.; Nafday, D.; Saha-Dasgupta, T. Manipulating the mechanical properties of Ti_2C MXene: Effect of substitutional doping. *Phys. Rev. B* **2017**, *95*, 184106. [[CrossRef](#)]
52. Andrew, R.C.; Mapasha, R.E.; Ukpong, A.M.; Chetty, N. Mechanical properties of graphene and boronitrene. *Phys. Rev. B* **2012**, *85*, 125428. [[CrossRef](#)]

53. Wu, D.; Wang, S.; Zhang, S.; Yuan, J.; Yang, B.; Chen, H. Highly negative Poisson's ratio in a flexible two-dimensional tungsten carbide monolayer. *Phys. Chem. Chem. Phys.* **2018**, *20*, 18924–18930. [[CrossRef](#)]
54. Isaacs, E.B.; Marianetti, C.A. Ideal strength and phonon instability of strained monolayer materials. *Phys. Rev. B* **2014**, *89*, 184111. [[CrossRef](#)]
55. Chen, S.; Fu, Z.; Zhang, H.; Legut, D.; Germann, T.C.; Zhang, Q.; Du, S.; Francisco, J.S.; Zhang, R. Surface Electrochemical Stability and Strain-Tunable Lithium Storage of Highly Flexible 2D Transition Metal Carbides. *Adv. Funct. Mater.* **2018**, *28*, 1804867. [[CrossRef](#)]
56. Radajewski, M.; Henschel, S.; Grützner, S.; Krüger, L.; Schimpf, C.; Chmelik, D.; Rafaja, D. Microstructure and mechanical properties of bulk TiN–AlN composites processed by FAST/SPS. *Ceram. Int.* **2016**, *42*, 10220–10227. [[CrossRef](#)]
57. Ivashchenko, V.I.; Turchi, P.E.A.; Gonis, A.; Ivashchenko, L.A.; Skrynskii, P.L. Electronic origin of elastic properties of titanium carbonitride alloys. *Met. Mater. Trans. A Phys. Met. Mater. Sci.* **2006**, *37*, 3391–3396. [[CrossRef](#)]
58. Yang, Q.; Lengauer, W.; Koch, T.; Scheerer, M.; Smid, I. Hardness and elastic properties of $Ti(C_xN_{1-x})$, $Zr(C_xN_{1-x})$ and $Hf(C_xN_{1-x})$. *J. Alloys Compd.* **2000**, *309*, L5–L9. [[CrossRef](#)]
59. Come, J.; Xie, Y.; Naguib, M.; Jesse, S.; Kalinin, S.V.; Gogotsi, Y.; Kent, P.R.C.; Balke, N. Nanoscale Elastic Changes in 2D $Ti_3C_2T_x$ (MXene) Pseudocapacitive Electrodes. *Adv. Energy Mater.* **2016**, *6*, 1–9. [[CrossRef](#)]
60. Borysiuk, V.N.; Mochalin, V.N.; Gogotsi, Y. Bending rigidity of two-dimensional titanium carbide (MXene) nanoribbons: A molecular dynamics study. *Comput. Mater. Sci.* **2018**, *143*, 418–424. [[CrossRef](#)]
61. Hu, T.; Yang, J.; Li, W.; Wang, X.; Li, C. Quantifying the rigidity of 2D carbides (MXenes). *Phys. Chem. Chem. Phys.* **2020**, *22*, 2115–2121. [[CrossRef](#)]
62. Suk, J.W.; Piner, R.D.; An, J.; Ruoff, R.S. Mechanical properties of monolayer graphene oxide. *ACS Nano* **2010**, *4*, 6557–6564. [[CrossRef](#)] [[PubMed](#)]
63. Liu, L.; Zhang, J.; Zhao, J.; Liu, F. Mechanical properties of graphene oxides. *Nanoscale* **2012**, *4*, 5910–5916. [[CrossRef](#)] [[PubMed](#)]
64. Wang, S.; Li, J.-X.; Du, Y.; Cui, C. First-principles study on structural, electronic and elastic properties of graphene-like hexagonal Ti_2C monolayer. *Comput. Mater. Sci.* **2014**, *83*, 290–293. [[CrossRef](#)]
65. Hu, T.; Hu, M.; Li, Z.; Zhang, H.; Zhang, C.; Wang, J.; Wang, X. Interlayer coupling in two-dimensional titanium carbide MXenes. *Phys. Chem. Chem. Phys.* **2016**, *18*, 20256–20260. [[CrossRef](#)]
66. Zhang, H.; Fu, Z.H.; Legut, D.; Germann, T.C.; Zhang, R.F. Stacking stability and sliding mechanism in weakly bonded 2D transition metal carbides by van der Waals force. *RSC Adv.* **2017**, *7*, 55912–55919. [[CrossRef](#)]
67. Zhang, D.; Ashton, M.; Ostadhosseini, A.; Van Duin, A.C.T.; Hennig, R.G.; Sinnott, S.B. Computational study of low interlayer friction in $Ti_{n+1}C_n$ ($n = 1, 2$, and 3) MXene. *ACS Appl. Mater. Interfaces* **2017**, *9*, 34467–34479. [[CrossRef](#)]
68. Li, Y.; Huang, S.; Wei, C.; Wu, C.; Mochalin, V.N. Adhesion of two-dimensional titanium carbides (MXenes) and graphene to silicon. *Nat. Commun.* **2019**, *10*, 1–8. [[CrossRef](#)]
69. Wu, Z.-S.; Feng, X.; Cheng, H.-M. Recent advances in graphene-based planar micro-supercapacitors for on-chip energy storage. *Natl. Sci. Rev.* **2014**, *1*, 277. [[CrossRef](#)]
70. Zhang, C.; Ma, Y.; Zhang, X.; Abdolhosseinzadeh, S.; Sheng, H.; Lan, W.; Pakdel, A.; Heier, J.; Nüesch, F. Two-Dimensional Transition Metal Carbides and Nitrides (MXenes): Synthesis, Properties, and Electrochemical Energy Storage Applications. *Energy Environ. Mater.* **2020**, *3*, 29–55. [[CrossRef](#)]
71. Zhang, C.; Nicolosi, V. Graphene and MXene-based transparent conductive electrodes and supercapacitors. *Energy Storage Mater.* **2019**, *16*, 102–125. [[CrossRef](#)]
72. Jiang, Q.; Lei, Y.; Liang, H.; Xi, K.; Xia, C.; Alshareef, H.N. Review of MXene electrochemical microsupercapacitors. *Energy Storage Mater.* **2020**, *27*, 78–95. [[CrossRef](#)]
73. Wang, K.; Zheng, B.; Mackinder, M.; Baule, N.; Qiao, H.; Jin, H.; Schuelke, T.; Fan, Q.H. Graphene wrapped MXene via plasma exfoliation for all-solid-state flexible supercapacitors. *Energy Storage Mater.* **2019**, *20*, 299–306. [[CrossRef](#)]
74. Rakhi, R.B.; Ahmed, B.; Hedhili, M.N.; Anjum, D.H.; Alshareef, H.N. Effect of Postetch Annealing Gas Composition on the Structural and Electrochemical Properties of Ti_2CT_x MXene Electrodes for Supercapacitor Applications. *Chem. Mater.* **2015**, *27*, 5314–5323. [[CrossRef](#)]

75. Tao, Q.; Dahlgqvist, M.; Lu, J.; Kota, S.; Meshkian, R.; Halim, J.; Palisaitis, J.; Hultman, L.; Barsoum, M.W.; Persson, P.O.Å.; et al. Two-dimensional Mo_{1.33}C MXene with divacancy ordering prepared from parent 3D laminate with in-plane chemical ordering. *Nat. Commun.* **2017**, *8*, 14949. [[CrossRef](#)] [[PubMed](#)]
76. Lukatskaya, M.R.; Mashtalir, O.; Ren, C.E.; Dall'Agnesse, Y.; Rozier, P.; Taberna, P.L.; Naguib, M.; Simon, P.; Barsoum, M.W.; Gogotsi, Y. Cation Intercalation and High Volumetric Capacitance of Two-Dimensional Titanium Carbide. *Science* **2013**, *341*, 1502–1505. [[CrossRef](#)]
77. Ghidui, M.; Lukatskaya, M.R.; Zhao, M.-Q.; Gogotsi, Y.; Barsoum, M.W. Conductive two-dimensional titanium carbide 'clay' with high volumetric capacitance. *Nature* **2014**, *516*, 78–81. [[CrossRef](#)] [[PubMed](#)]
78. Lukatskaya, M.R.; Kota, S.; Lin, Z.; Zhao, M.-Q.; Shpigel, N.; Levi, M.D.; Halim, J.; Taberna, P.-L.; Barsoum, M.W.; Simon, P.; et al. Ultra-high-rate pseudocapacitive energy storage in two-dimensional transition metal carbides. *Nat. Energy* **2017**, *2*, 1–6. [[CrossRef](#)]
79. Shan, Q.; Mu, X.; Alhabeab, M.; Shuck, C.E.; Pang, D.; Zhao, X.; Chu, X.-F.; Wei, Y.; Du, F.; Chen, G.; et al. Two-dimensional vanadium carbide (V₂C) MXene as electrode for supercapacitors with aqueous electrolytes. *Electrochem. Commun.* **2018**, *96*, 103–107. [[CrossRef](#)]
80. Halim, J.; Kota, S.; Lukatskaya, M.R.; Naguib, M.; Zhao, M.-Q.; Moon, E.J.; Pitock, J.; Nanda, J.; May, S.J.; Gogotsi, Y.; et al. Synthesis and Characterization of 2D Molybdenum Carbide (MXene). *Adv. Funct. Mater.* **2016**, *26*, 3118–3127. [[CrossRef](#)]
81. Dall'Agnesse, Y.; Lukatskaya, M.R.; Cook, K.M.; Taberna, P.-L.; Gogotsi, Y.; Simon, P. High capacitance of surface-modified 2D titanium carbide in acidic electrolyte. *Electrochem. Commun.* **2014**, *48*, 118–122. [[CrossRef](#)]
82. Zhan, C.; Sun, W.; Kent, P.R.C.; Naguib, M.; Gogotsi, Y.; Jiang, D.-E. Computational Screening of MXene Electrodes for Pseudocapacitive Energy Storage. *J. Phys. Chem. C* **2019**, *123*, 315–321. [[CrossRef](#)]
83. Zhan, C.; Naguib, M.; Lukatskaya, M.; Kent, P.R.; Gogotsi, Y.; Jiang, D.-E. Understanding the MXene pseudocapacitance. *J. Phys. Chem. Lett.* **2018**, *9*, 1223–1228. [[CrossRef](#)] [[PubMed](#)]
84. Boota, M.; Anasori, B.; Voigt, C.; Zhao, M.Q.; Barsoum, M.W.; Gogotsi, Y. Pseudocapacitive Electrodes Produced by Oxidant-Free Polymerization of Pyrrole between the Layers of 2D Titanium Carbide (MXene). *Adv. Mater. (Deerfield Beach, Fla)* **2016**, *28*, 1517–1522. [[CrossRef](#)]
85. Wang, X.; Kajiyama, S.; Iinuma, H.; Hosono, E.; Oro, S.; Moriguchi, I.; Okubo, M.; Yamada, A. Pseudocapacitance of MXene nanosheets for high-power sodium-ion hybrid capacitors. *Nat. Commun.* **2015**, *6*, 6544. [[CrossRef](#)]
86. Li, H.; Hou, Y.; Wang, F.; Lohe, M.R.; Zhuang, X.; Niu, L.; Feng, X. Flexible All-Solid-State Supercapacitors with High Volumetric Capacitances Boosted by Solution Processable MXene and Electrochemically Exfoliated Graphene. *Adv. Energy Mater.* **2017**, *7*, 1601847. [[CrossRef](#)]
87. Tang, Q.; Zhou, Z.; Shen, P. Are MXenes Promising Anode Materials for Li Ion Batteries? Computational Studies on Electronic Properties and Li Storage Capability of Ti₃C₂ and Ti₃C₂X₂ (X = F, OH) Monolayer. *J. Am. Chem. Soc.* **2012**, *134*, 16909–16916. [[CrossRef](#)] [[PubMed](#)]
88. Wang, L.; Zhang, H.; Wang, B.; Shen, C.; Zhang, C.; Hu, Q.; Zhou, A.; Liu, B. Synthesis and electrochemical performance of Ti₃C₂T_x with hydrothermal process. *Electron. Mater. Lett.* **2016**, *12*, 702–710. [[CrossRef](#)]
89. Couly, C.; Alhabeab, M.; Van Aken, K.L.; Kurra, N.; Gomes, L.; Navarro-Suárez, A.M.; Anasori, B.; Alshareef, H.N.; Gogotsi, Y. Asymmetric Flexible MXene-Reduced Graphene Oxide Micro-Supercapacitor. *Adv. Electron. Mater.* **2018**, *4*, 1700339. [[CrossRef](#)]
90. Fu, Q.; Wang, X.; Zhang, N.; Wen, J.; Li, L.; Gao, H.; Zhang, X. Self-assembled Ti₃C₂T_x/SCNT composite electrode with improved electrochemical performance for supercapacitor. *J. Colloid Interface Sci.* **2018**, *511*, 128–134. [[CrossRef](#)]
91. Jiang, Q.; Wu, C.; Wang, Z.; Wang, A.C.; He, J.-H.; Wang, Z.L.; Alshareef, H.N. MXene electrochemical microsupercapacitor integrated with triboelectric nanogenerator as a wearable self-charging power unit. *Nano Energy* **2018**, *45*, 266–272. [[CrossRef](#)]
92. Xia, Q.X.; Shinde, N.M.; Yun, J.M.; Zhang, T.; Mane, R.S.; Mathur, S.; Kim, K.H. Bismuth Oxychloride/MXene symmetric supercapacitor with high volumetric energy density. *Electrochim. Acta* **2018**, *271*, 351–360. [[CrossRef](#)]
93. Zhang, C.; Kremer, M.P.; Seral-Ascaso, A.; Park, S.-H.; McEvoy, N.; Anasori, B.; Gogotsi, Y.; Nicolosi, V. Stamping of Flexible, Coplanar Micro-Supercapacitors Using MXene Inks. *Adv. Funct. Mater.* **2018**, *28*, 1705506. [[CrossRef](#)]

94. Hu, M.; Li, Z.; Zhang, H.; Hu, T.; Zhang, C.; Wu, Z.; Wang, X. Self-assembled Ti₃C₂T_x MXene film with high gravimetric capacitance. *Chem. Commun.* **2015**, *51*, 13531–13533. [[CrossRef](#)]
95. Tang, Y.; Zhu, J.; Yang, C.; Wang, F. Enhanced Capacitive Performance Based on Diverse Layered Structure of Two-Dimensional Ti₃C₂MXene with Long Etching Time. *J. Electrochem. Soc.* **2016**, *163*, A1975–A1982. [[CrossRef](#)]
96. Mashtalir, O.; Lukatskaya, M.R.; Kolesnikov, A.I.; Raymundo-Piñero, E.; Naguib, M.; Barsoum, M.W.; Gogotsi, Y. The effect of hydrazine intercalation on the structure and capacitance of 2D titanium carbide (MXene). *Nanoscale* **2016**, *8*, 9128–9133. [[CrossRef](#)] [[PubMed](#)]
97. Fu, Q.; Wen, J.; Zhang, N.; Wu, L.; Zhang, M.; Lin, S.; Gao, H.; Zhang, X. Free-standing Ti₃C₂T_x electrode with ultrahigh volumetric capacitance. *RSC Adv.* **2017**, *7*, 11998–12005. [[CrossRef](#)]
98. Wen, Y.; Rufford, T.E.; Chen, X.; Li, N.; Lyu, M.; Dai, L.; Wang, L. Nitrogen-doped Ti₃C₂T_x MXene electrodes for high-performance supercapacitors. *Nano Energy* **2017**, *38*, 368–376. [[CrossRef](#)]
99. Kurra, N.; Ahmed, B.; Gogotsi, Y.; Alshareef, H.N. MXene-on-Paper Coplanar Microsupercapacitors. *Adv. Energy Mater.* **2016**, *6*, 1601372. [[CrossRef](#)]
100. Wang, Y.; Dou, H.; Wang, J.; Ding, B.; Xu, Y.; Chang, Z.; Hao, X. Three-dimensional porous MXene/layered double hydroxide composite for high performance supercapacitors. *J. Power Sources* **2016**, *327*, 221–228. [[CrossRef](#)]
101. Li, J.; Yuan, X.; Lin, C.; Yang, Y.; Xu, L.; Du, X.; Xie, J.; Lin, J.; Sun, J. Achieving High Pseudocapacitance of 2D Titanium Carbide (MXene) by Cation Intercalation and Surface Modification. *Adv. Energy Mater.* **2017**, *7*, 1602725. [[CrossRef](#)]
102. Zhao, M.-Q.; Ren, C.E.; Ling, Z.; Lukatskaya, M.R.; Zhang, C.; Van Aken, K.L.; Barsoum, M.W.; Gogotsi, Y. Flexible MXene/Carbon Nanotube Composite Paper with High Volumetric Capacitance. *Adv. Mater.* **2015**, *27*, 339–345. [[CrossRef](#)] [[PubMed](#)]
103. Yan, J.; Ren, C.E.; Maleski, K.; Hatter, C.B.; Anasori, B.; Urbankowski, P.; Sarycheva, A.; Gogotsi, Y. Flexible MXene/Graphene Films for Ultrafast Supercapacitors with Outstanding Volumetric Capacitance. *Adv. Funct. Mater.* **2017**, *27*, 1701264. [[CrossRef](#)]
104. Dall’Agnese, Y.; Rozier, P.; Taberna, P.-L.; Gogotsi, Y.; Simon, P. Capacitance of two-dimensional titanium carbide (MXene) and MXene/carbon nanotube composites in organic electrolytes. *J. Power Sources* **2016**, *306*, 510–515. [[CrossRef](#)]
105. Yan, P.; Zhang, R.; Jia, J.; Wu, C.; Zhou, A.; Xu, J.; Zhang, X. Enhanced supercapacitive performance of delaminated two-dimensional titanium carbide/carbon nanotube composites in alkaline electrolyte. *J. Power Sources* **2015**, *284*, 38–43. [[CrossRef](#)]
106. Zhu, J.; Tang, Y.; Yang, C.; Wang, F.; Cao, M. Composites of TiO₂Nanoparticles Deposited on Ti₃C₂MXene Nanosheets with Enhanced Electrochemical Performance. *J. Electrochem. Soc.* **2016**, *163*, A785–A791. [[CrossRef](#)]
107. Tian, Y.; Yang, C.; Que, W.; Liu, X.; Yin, X.; Kong, L.B. Flexible and freestanding 2D titanium carbide film decorated with manganese oxide nanoparticles as a high volumetric capacity electrode for supercapacitor. *J. Power Sources* **2017**, *359*, 332–339. [[CrossRef](#)]
108. Zhu, M.; Huang, Y.; Deng, Q.; Zhou, J.; Pei, Z.; Xue, Q.; Huang, Y.; Wang, Z.; Li, H.; Huang, Q.; et al. Highly Flexible, Freestanding Supercapacitor Electrode with Enhanced Performance Obtained by Hybridizing Polypyrrole Chains with MXene. *Adv. Energy Mater.* **2016**, *6*, 1600969. [[CrossRef](#)]
109. Luo, J.; Zhang, W.; Yuan, H.; Jin, C.; Zhang, L.; Huang, H.; Liang, C.; Xia, Y.; Zhang, J.; Gan, Y.; et al. Pillared Structure Design of MXene with Ultralarge Interlayer Spacing for High-Performance Lithium-Ion Capacitors. *ACS Nano* **2017**, *11*, 2459–2469. [[CrossRef](#)]
110. Lin, Z.; Barbara, D.; Taberna, P.-L.; Van Aken, K.L.; Anasori, B.; Gogotsi, Y.; Simon, P. Capacitance of Ti₃C₂T_x MXene in ionic liquid electrolyte. *J. Power Sources* **2016**, *326*, 575–579. [[CrossRef](#)]
111. Wang, X.; Mathis, T.S.; Li, K.; Lin, Z.; Vlcek, L.; Torita, T.; Osti, N.C.; Hatter, C.; Urbankowski, P.; Sarycheva, A.; et al. Influences from solvents on charge storage in titanium carbide MXenes. *Nat. Energy* **2019**, *4*, 241–248. [[CrossRef](#)]
112. Sobolčiak, P.; Ali, A.; Hassan, M.K.; Helal, M.I.; Tanvir, A.; Popelka, A.; Al-Maadeed, M.A.; Krupa, I.; Mahmoud, K.A. 2D Ti₃C₂T_x (MXene)-reinforced polyvinyl alcohol (PVA) nanofibers with enhanced mechanical and electrical properties. *PLoS ONE* **2017**, *12*, e0183705. [[CrossRef](#)] [[PubMed](#)]

113. Wang, N.-N.; Wang, H.; Wang, Y.-Y.; Wei, Y.-H.; Si, J.-Y.; Yuen, A.C.Y.; Xie, J.-S.; Yu, B.; Zhu, S.-E.; Lu, H.-D.; et al. Robust, Lightweight, Hydrophobic, and Fire-Retarded Polyimide/MXene Aerogels for Effective Oil/Water Separation. *ACS Appl. Mater. Interfaces* **2019**, *11*, 40512–40523. [[CrossRef](#)] [[PubMed](#)]
114. Liu, J.; Zhang, L.; Li, C. Highly Stable, Transparent, and Conductive Electrode of Solution-Processed Silver Nanowire-Mxene for Flexible Alternating-Current Electroluminescent Devices. *Ind. Eng. Chem. Res.* **2019**, *58*, 21485–21492. [[CrossRef](#)]
115. Sambyal, P.; Iqbal, A.; Hong, J.; Kim, H.; Kim, M.-K.; Hong, S.M.; Han, M.; Gogotsi, Y.; Koo, C.M. Ultralight and Mechanically Robust $Ti_3C_2T_x$ Hybrid Aerogel Reinforced by Carbon Nanotubes for Electromagnetic Interference Shielding. *ACS Appl. Mater. Interfaces* **2019**, *11*, 38046–38054. [[CrossRef](#)] [[PubMed](#)]
116. Abualrejal, M.M.; Eid, K.; Tian, R.; Liu, L.; Chen, H.; Abdullah, A.M.; Wang, Z. Rational synthesis of three-dimensional core–double shell upconversion nanodendrites with ultrabright luminescence for bioimaging application. *Chem. Sci.* **2019**, *10*, 7591–7599. [[CrossRef](#)]
117. Abualrejal, M.M.; Eid, K.; Abdullah, A.M.; Numan, A.A.; Chen, H.; Zhang, H.; Wang, Z. Smart design of exquisite multidimensional multilayered sand-clock-like upconversion nanostructures with ultrabright luminescence as efficient luminescence probes for bioimaging application. *Microchim. Acta* **2020**, *187*, 1–13. [[CrossRef](#)]
118. Wu, F.; Eid, K.; Abdullah, A.M.; Niu, W.; Wang, C.; Lan, Y.; Elzatahry, A.A.; Xu, G. Unveiling One-Pot Template-Free Fabrication of Exquisite Multidimensional PtNi Multicube Nanoarchitectonics for the Efficient Electrochemical Oxidation of Ethanol and Methanol with a Great Tolerance for CO. *ACS Appl. Mater. Interfaces* **2020**, *12*, 31309–31318. [[CrossRef](#)]
119. Eid, K.; Sliem, M.H.; Jlassi, K.; Eldesoky, A.S.; Abdo, G.G.; Al-Qaradawi, S.Y.; Sharaf, M.A.; Abdullah, A.M.; Elzatahry, A.A. Precise fabrication of porous one-dimensional gC₃N₄ nanotubes doped with Pd and Cu atoms for efficient CO oxidation and CO₂ reduction. *Inorg. Chem. Commun.* **2019**, *107*, 107460. [[CrossRef](#)]



© 2020 by the authors. Licensee MDPI, Basel, Switzerland. This article is an open access article distributed under the terms and conditions of the Creative Commons Attribution (CC BY) license (<http://creativecommons.org/licenses/by/4.0/>).